

1 Supporting Information Text

1. Minimization of custom Lyapunov function Γ

In this section we will give a detailed derivation of the dynamic equations for the networks' radii and an introduction to the common notations used. Having established a fully connected graph which we will use for our simulations we choose an arbitrary direction for each edge. Every cyclic path, meaning a progression of incident edges which starts and terminates at the same node, we will refer to as circle or loop. This special class of networks are often referred to as Kirchhoff or lumped networks. We formulate the constraint,

$$\sum_e B_{je} f_e = s_j \Leftrightarrow \mathbf{B} \cdot \mathbf{f} = \mathbf{s} \quad [1]$$

with $\mathbf{s} \in \mathbb{R}^n$, $\mathbf{f} \in \mathbb{R}^m$, $\mathbf{B} \in \mathbb{R}^{n \times m}$ referred to as current law, which can be interpreted as a mass conversation law for every vertex. Nodes with positive values of s_j are to be referred to as sources, negative ones as sinks. \mathbf{B} denotes the graph's incidence matrix. This setup is also referred to as value boundary problem (Neumann problem (1)), with terminal nodes ($s_j \neq 0$) and internal nodes ($s_j = 0$). In linear lumped systems one can derive Ohm's law for every edge,

$$f_e = c_e \Delta p_e \Leftrightarrow \mathbf{f} = \mathbf{C} \cdot \Delta \mathbf{p} \quad [2]$$

with the conductivity matrix $\mathbf{C} \in \mathbb{R}^{m \times m}$ being diagonal $C_{ef} = c_e \delta_{ef}$. From the Hagen-Poiseuille law we know the conductivities to be $c_e = \frac{\pi r_e^4}{8\eta l_e}$, meaning the resulting flow rate is crucially dependent on the vessel's radius. From the current law Eq. (1) in combination with Ohm's law Eq. (2) one may further show that the sum over all in and outflows of the system vanishes(2), i.e. $\sum_j s_j = 0$. Further combining Eq. (1) and Eq. (2) we can see that:

$$\mathbf{B} \cdot \mathbf{C} \cdot \Delta \mathbf{p} = \mathbf{s} \quad [3]$$

The $n \times m$ matrix $\mathbf{B} \cdot \mathbf{C}$ is non-invertible as it is a non-square matrix of rank $n - 1$. A solution may however be constructed by means of the generalized inverse (denoted here as $[\cdot]^\dagger$ (3)). Via the dissipation minimization argument one can deduce the potential vector to be:

$$\Delta \mathbf{p} = \mathbf{C}^{-1/2} [\mathbf{B} \cdot \mathbf{C}^{1/2}]^\dagger \mathbf{s} \quad [4]$$

3 Proving equation Eq. (4) to be the unique solution which minimizes the system's dissipation is given in (4, 5). On a further
4 note, we'd like to mention that this calculation is not just restricted to laminar viscous flows but any stationary transport
5 system, e.g. diffusion. This phenomenon is also referred to as the Thomson principle (6, 7).
6

The optimization of the flow system will require the formulation of a positive definite cost function. For convenience we will write a Lyapunov function Γ as

$$\Gamma = P + P' + E \quad [5]$$

$$\text{with } P = \sum_e l \left[\frac{8\eta}{\pi} \frac{f_e^2}{r_e^4} + a r_e^2 \right] \quad [6]$$

$$\text{and } P' = \sum_{e'} l' \left[\frac{8\eta'}{\pi} \frac{f_{e'}^2}{r_{e'}^4} + a' r_{e'}^2 \right] \quad [7]$$

We may further use the vectorial notation for dissipation-volume terms P, P' , using Ohms law to formulate it in terms of the nodal sinks/sources (here just for P, derivation for P' is performed analogously),

$$P = l [\mathbf{f}^T \mathbf{K}^{-1} \mathbf{f} + q \text{Tr}(\mathbf{K}^{1/2})] \quad [8]$$

$$= l [\mathbf{s}^T [\mathbf{B}^T \mathbf{K} \mathbf{B}]^\dagger \mathbf{s} + q \text{Tr}(\mathbf{K}^{1/2})] \quad [9]$$

with $q = a \left(\frac{8\eta}{\pi}\right)^{1/2}$ and $k_e = \frac{\pi r_e^4}{8\eta}$ as entries of the diagonal \mathbf{K} . We used $\Delta \varphi = \mathbf{K}^{-1/2} [\mathbf{B} \cdot \mathbf{K}^{1/2}]^\dagger \mathbf{s}$ and $\mathbf{f} = \mathbf{K} \cdot \Delta \varphi$. We calculate the (pseudo-)time derivatives of P to be

$$\begin{aligned} \frac{1}{l} \frac{dP}{dh} &= \mathbf{s}^T \partial_h [\mathbf{B} \cdot \mathbf{K} \cdot \mathbf{B}^T]^\dagger \mathbf{s} \\ &+ 2\mathbf{s}^T [\mathbf{B} \cdot \mathbf{K} \cdot \mathbf{B}^T]^\dagger \partial_h \mathbf{s} + q \partial_h \text{Tr}(\mathbf{K}^{1/2}) \end{aligned} \quad [10]$$

The derivative of the generalized inverse $\mathbf{B} \cdot \mathbf{K} \cdot \mathbf{B}^T = \mathbf{A}$ being (8),

$$\begin{aligned} \partial_h \mathbf{A}^\dagger &= -\mathbf{A}^\dagger (\mathbf{B} \cdot \partial_h \mathbf{K} \cdot \mathbf{B}^T) \mathbf{A}^\dagger \\ &\quad + [\mathbf{I} - \mathbf{A}^\dagger \cdot \mathbf{A}] (\mathbf{B} \cdot \partial_h \mathbf{K} \cdot \mathbf{B}^T) \mathbf{A}^{T\dagger} \cdot \mathbf{A}^\dagger \\ &\quad + \mathbf{A}^\dagger \cdot \mathbf{A}^{T\dagger} (\mathbf{B}^T \cdot \partial_h \mathbf{K} \cdot \mathbf{B}) [\mathbf{I} - \mathbf{A} \cdot \mathbf{A}^\dagger] \end{aligned} \quad [11]$$

Fortunately the projector terms vanish as we have,

$$\mathbf{s}^T [\mathbf{I} - \mathbf{A}^\dagger \cdot \mathbf{A}] = 0 \text{ and } [\mathbf{I} - \mathbf{A} \cdot \mathbf{A}^\dagger] \mathbf{s} = 0 \quad [12]$$

Together with the identity $\mathbf{A}^\dagger = (\mathbf{A}^T)^\dagger$ the total time-derivative of P becomes,

$$\begin{aligned} \frac{1}{l} \frac{dP}{dh} &= -\mathbf{s}^T \mathbf{A}^{T\dagger} (\mathbf{B} \cdot \partial_h \mathbf{K} \cdot \mathbf{B}^T) \mathbf{A}^\dagger \mathbf{s} \\ &\quad + 2\mathbf{s}^T \mathbf{A}^\dagger \partial_h \mathbf{s} + q \partial_h \text{Tr} (\mathbf{K}^{1/2}) \end{aligned} \quad [13]$$

With partial derivatives simplifying this formula as:

$$\partial_h \text{Tr} (\mathbf{K}^{1/2}) = \frac{1}{2} \text{Tr} (\mathbf{K}^{-1/2} \cdot \partial_h \mathbf{K}) \quad [14]$$

$$\partial_h \mathbf{s} = 0 \quad [15]$$

As $\Delta\varphi = \mathbf{B}^T \cdot \mathbf{A}^\dagger \mathbf{s}$, we may write the total time-derivative as

$$\frac{1}{l} \frac{dP}{dh} = -\Delta\varphi^T \cdot \partial_h \mathbf{K} \cdot \Delta\varphi + \frac{q}{2} \text{Tr} (\mathbf{K}^{-1/2} \partial_h \mathbf{K}) \quad [16]$$

With $\partial_h K_{ee} = \frac{\pi r_e^3}{2\eta} \partial_h r_e$ and re-substituting q this becomes

$$\frac{1}{l} \frac{dP}{dh} = \frac{\pi}{2\eta} \sum_e r_e \left[\frac{4a\eta}{\pi} - \Delta\varphi_e^2 r_e^2 \right] \partial_h r_e \quad [17]$$

The coupling component's derivative E may be calculated with partial derivatives,

$$\frac{E}{dh} = \frac{b(\varepsilon - 1)}{2} \left[\sum_{ee'} F_{ee'} \Delta r_{ee'}^{-\varepsilon} \partial_h r_e + \sum_{e'e} F_{e'e} \Delta r_{e'e}^{-\varepsilon} \partial_h r_{e'} \right] \quad [18]$$

so combining Eq. (17) and Eq. (18) we get for the total derivative of Γ ,

$$\begin{aligned} \frac{d\Gamma}{dh} &= \frac{\pi l}{2\eta} \sum_e r_e \left[\frac{4a\eta}{\pi} - \Delta\varphi_e^2 r_e^2 \right] r_e \partial_h r_e \\ &\quad + \frac{\pi l'}{2\eta'} \sum_{e'} \left[\frac{4a'\eta'}{\pi} - \Delta\varphi_{e'}^2 r_{e'}^2 \right] r_{e'} \partial_h r_{e'} \\ &\quad + \frac{b(\varepsilon - 1)}{2} \left[\sum_e F_{ee'} \Delta r_{ee'}^{-\varepsilon} \partial_h r_e + \sum_{e'} F_{e'e} \Delta r_{e'e}^{-\varepsilon} \partial_h r_{e'} \right] \end{aligned} \quad [19]$$

We then acquire the ODE system presented in the main body of our paper by setting $\alpha = \frac{4a\eta}{\pi}$ and $\beta = \frac{b(\varepsilon-1)\eta}{\pi l}$ and α' , β' accordingly,

$$\begin{aligned} \frac{d\Gamma}{dh} &= \frac{\pi l}{2\eta} \sum_e \left([\alpha - \Delta\varphi_e^2 r_e^2] r_e + \beta \sum_{e'} F_{ee'} \Delta r_{ee'}^{-\varepsilon} \right) \partial_h r_e \\ &\quad + \frac{\pi l'}{2\eta'} \sum_{e'} \left([\alpha' - \Delta\varphi_{e'}^2 r_{e'}^2] r_{e'} + \beta' \sum_e F_{e'e} \Delta r_{e'e}^{-\varepsilon} \right) \partial_h r_{e'} \end{aligned} \quad [20]$$

To find a local minimum of Γ when progressing through (pseudo-)time h we we have to ensure that $d\Gamma \leq 0$. So we may minimize the Lyapunov function, with auxillary functions χ , $\chi' \geq 0$ by choosing

$$\partial_h r_e = \chi \left([\Delta\varphi_e^2 r_e^2 - \alpha] r_e - \beta \sum_{e'} F_{ee'} \Delta r_{ee'}^{-\varepsilon} \right) \quad [21]$$

$$\partial_h r_{e'} = \chi' \left([\Delta\varphi_{e'}^2 r_{e'}^2 - \alpha'] r_{e'} - \beta' \sum_e F_{e'e} \Delta r_{e'e}^{-\varepsilon} \right) \quad [22]$$

7 2. Uncorrelated and coupled flow fluctuations

In this section we give a detailed derivation of the analytic form of the mean squared pressure in case of uncorrelated, identically distributed sink fluctuations as introduced in (9). When considering the sink conditions as well as the source constraint defined in the theory section, we may write the moments as,

$$\langle s_j \rangle = \mu \quad [23]$$

$$\langle s_0 \rangle = - \left\langle \sum_{j>0} s_j \right\rangle = (1-n) \mu \quad [24]$$

$$\langle s_j s_k \rangle = \delta_{jk} \sigma^2 + \mu^2 \text{ if } j, k > 0 \quad [25]$$

$$\langle s_0^2 \rangle = \left\langle \sum_{j,k>0} s_j s_k \right\rangle = (n-1) \sigma^2 + (n-1)^2 \mu^2 \quad [26]$$

$$\langle s_0 s_k \rangle = - \left\langle \sum_{j>0} s_j s_k \right\rangle = -(n-1) \mu^2 - \sigma^2 \quad [27]$$

Hence we may calculate the squared-mean pressure by using the auxillary conductivity tensor $\mathbf{A}_{jk}^e = \mathbf{K}_{ee}^{-1} [\mathbf{B} \cdot \mathbf{K}^{1/2}]_{ej}^\dagger [\mathbf{B} \cdot \mathbf{K}^{1/2}]_{ek}^\dagger$ as,

$$\langle \Delta \varphi_e^2 \rangle = \sum_{jk} \mathbf{A}_{jk}^e \langle s_j s_k \rangle \quad [28]$$

$$\begin{aligned} &= \mathbf{A}_{00}^e \langle s_0^2 \rangle + 2 \sum_{j>0} \mathbf{A}_{j0}^i \langle s_0 s_j \rangle + \sum_{j,k>0} \mathbf{A}_{jk}^i \langle s_j s_k \rangle \\ &= \mathbf{A}_{00}^e (n-1) [(n-1) \mu^2 + \sigma^2] \\ &\quad - 2 \sum_{j>0} \mathbf{A}_{j0}^e [(n-1) \mu^2 + \sigma^2] \\ &\quad + \sum_{j,k>0} \mathbf{A}_{jk}^e [\delta_{jk} \sigma^2 + \mu^2] \end{aligned} \quad [29]$$

$$\begin{aligned} &= \sum_{j,k} \mathbf{A}_{jk}^e (n-1) [(n-1) \mu^2 + \sigma^2] \delta_{0j} \delta_{0k} \\ &\quad - \sum_{j,k} \mathbf{A}_{jk}^e [(n-1) \mu^2 + \sigma^2] [(1-\delta_{0k}) \delta_{0j} + (1-\delta_{0j}) \delta_{0k}] \\ &\quad + \sum_{j,k} \mathbf{A}_{jk}^e [\delta_{jk} \sigma^2 + \mu^2] (1-\delta_{0j}) (1-\delta_{0k}) \end{aligned} \quad [30]$$

Ordering the terms for μ and σ respectively we can acquire the coefficient matrices \mathbf{U} and \mathbf{V} ,

$$\begin{aligned} \langle \Delta \varphi_e^2 \rangle &= \sum_{j,k} \mathbf{A}_{jk}^e \mu^2 [(1-\delta_{0j})(1-\delta_{0k}) + \delta_{0j} \delta_{0k} (n-1)^2 - (n-1)(\delta_{0j}(1-\delta_{0k}) + \delta_{0k}(1-\delta_{0j}))] \\ &\quad + \sum_{j,k} \mathbf{A}_{jk}^e \sigma^2 [(1-\delta_{0k})(1-\delta_{0j}) \delta_{jk} - \delta_{0j}(1-\delta_{0k}) - \delta_{0k}(1-\delta_{0j}) + (n-1) \delta_{0j} \delta_{0k}] \end{aligned} \quad [31]$$

$$\begin{aligned} &= \sum_{j,k} \mathbf{A}_{jk}^e \mu^2 [1 + \delta_{0j} \delta_{0k} n^2 - n(\delta_{0j} + \delta_{0k})] \\ &\quad + \sum_{j,k} \mathbf{A}_{jk}^e \sigma^2 [\delta_{jk} + (n+1 + \delta_{jk}) \delta_{0j} \delta_{0k} - (1 + \delta_{jk})(\delta_{0j} + \delta_{0k})] \end{aligned} \quad [32]$$

We further suggest to expand this ansatz by introducing additional sources which act as clones of the very first one, i.e. we will have $s_p = s_q$ using the indices p, q for sources and u, v for sinks. Then conditions Eq. (24), Eq. (26), Eq. (27) will become for a

sources and b sinks (with $a + b = n$),

$$\left\langle \sum_p s_p \right\rangle = - \left\langle \sum_u s_u \right\rangle = -b\mu \rightarrow \langle s_p \rangle = -\frac{b}{a}\mu \quad [33]$$

$$\langle s_p s_q \rangle = \frac{1}{a^2} \left\langle \sum_{u,v} s_u s_v \right\rangle = \frac{1}{a^2} (b\sigma^2 + b^2\mu^2) \quad [34]$$

$$\langle s_p s_u \rangle = -\frac{1}{a} \left\langle \sum_v s_v s_u \right\rangle = -\frac{1}{a} (b\mu^2 - \sigma^2) \quad [35]$$

And hence we may calculate the mean squared pressure and its coefficient matrices respectively as,

$$\begin{aligned} \langle \Delta\varphi_e^2 \rangle &= \sum_{j,k} \mathbf{A}_{jk}^e \mu^2 \left[\frac{b^2}{a^2} \sum_{pq} \delta_{pj} \delta_{qk} - \frac{b}{a} \sum_{pu} (\delta_{pj} \delta_{uk} + \delta_{uj} \delta_{pk}) + \sum_{uv} \delta_{uj} \delta_{vk} \right] \\ &+ \sum_{j,k} \mathbf{A}_{jk}^e \sigma^2 \left[\frac{b}{a^2} \sum_{pq} \delta_{pj} \delta_{qk} - \frac{1}{a} \sum_{pu} (\delta_{pj} \delta_{uk} + \delta_{uj} \delta_{pk}) + \sum_{uv} \delta_{uj} \delta_{vk} \delta_{uv} \right] \end{aligned} \quad [36]$$

In case of more elaborate configurations as proposed in (10), i.e. spatially correlated \mathbf{s} -configurations, the authors suggested using the arithmetic average of a set of potential sink realizations \mathbf{s}_x to calculate the mean squared flow as,

$$\langle f_e^2 \rangle = \sum_x f_{e,x}^2 \text{ with } \mathbf{f}_x = \mathbf{B}^T (\mathbf{B}\mathbf{C}\mathbf{B}^T)^\dagger \mathbf{s}_x \quad [37]$$

which demands the calculation of each single flow realization with the Moore-Penrose inverse. This problem may be more elegantly formulated for the analogue mean squared pressure, using Eq. (28) to write,

$$\begin{aligned} \langle \Delta\varphi_e^2 \rangle &= [\mathbf{D} \cdot \langle \mathbf{s} \otimes \mathbf{s} \rangle \cdot \mathbf{D}^T]_{ee} \\ \text{with } \mathbf{D} &= \mathbf{B}^T (\mathbf{B}\mathbf{K}\mathbf{B}^T)^\dagger. \end{aligned} \quad [38]$$

This allows us to more quickly handle averages using just one arithmetic mean over a set of sink-source realizations \mathbf{s}_q as

$$\langle \mathbf{s} \otimes \mathbf{s} \rangle = \frac{1}{N} \sum_x \mathbf{s}_x \otimes \mathbf{s}_x \quad [39]$$

8 which might improve the computation of Eq. (28) in case of small iteration numbers x .

9 3. Limit case of uncoupled flow networks

From the rescaled ODE set of two coupled networks we may easily reproduce the uncoupled case for the two networks by setting $\lambda_1 = \lambda'_1 = 0$. With focus on just one network we have the radii adaptation,

$$\begin{aligned} \partial_h \rho_e &= \lambda_0 [\rho_e^2 \langle \Delta \Phi_e^2 \rangle - \lambda_2] \rho_e \\ \text{with } \langle \Delta \Phi_e^2 \rangle &= \sum_{jk} \alpha_{jk}^e [U_{jk} + \lambda_3 V_{jk}] \end{aligned} \quad [40]$$

10 which resembles the gradient flow driven optimization model proposed in the original Hu-Cai model (11) in combination with
 11 the flow fluctuation notation proposed in (9). We calculate the adaptation of simple cubic networks with a single corner source
 12 node (sinks otherwise) for a systematic scan of λ_2, λ_3 , see Figure S1 and S2. In particular we can show that in agreement with
 13 (11) only an increase in the flow to fluctuation ratio λ_3 results in an increase of nullity and that the continuous transition
 14 observed is independent of the systems effective volume penalty λ_2 , see Figure S1. The system's transition is logarithmic for
 15 $\lambda_3 > 1$ and saturates for large λ_3 , as was shown in the main body of this study. This transition is qualitatively conserved for
 16 all other periodic lattices, i.e. fcc, bcc and diamond lattice follow the same transition type.

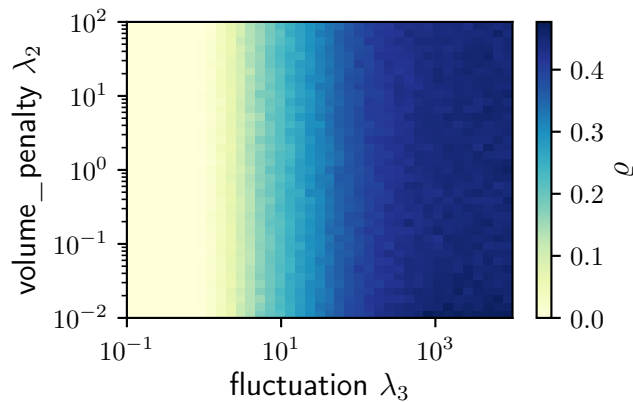


Fig. S1. Network nullity state diagram for (λ_2, λ_3) : No dependency of volume penalty λ_2 , onset of fluctuation induced loops is controlled by rate of fluctuation λ_3

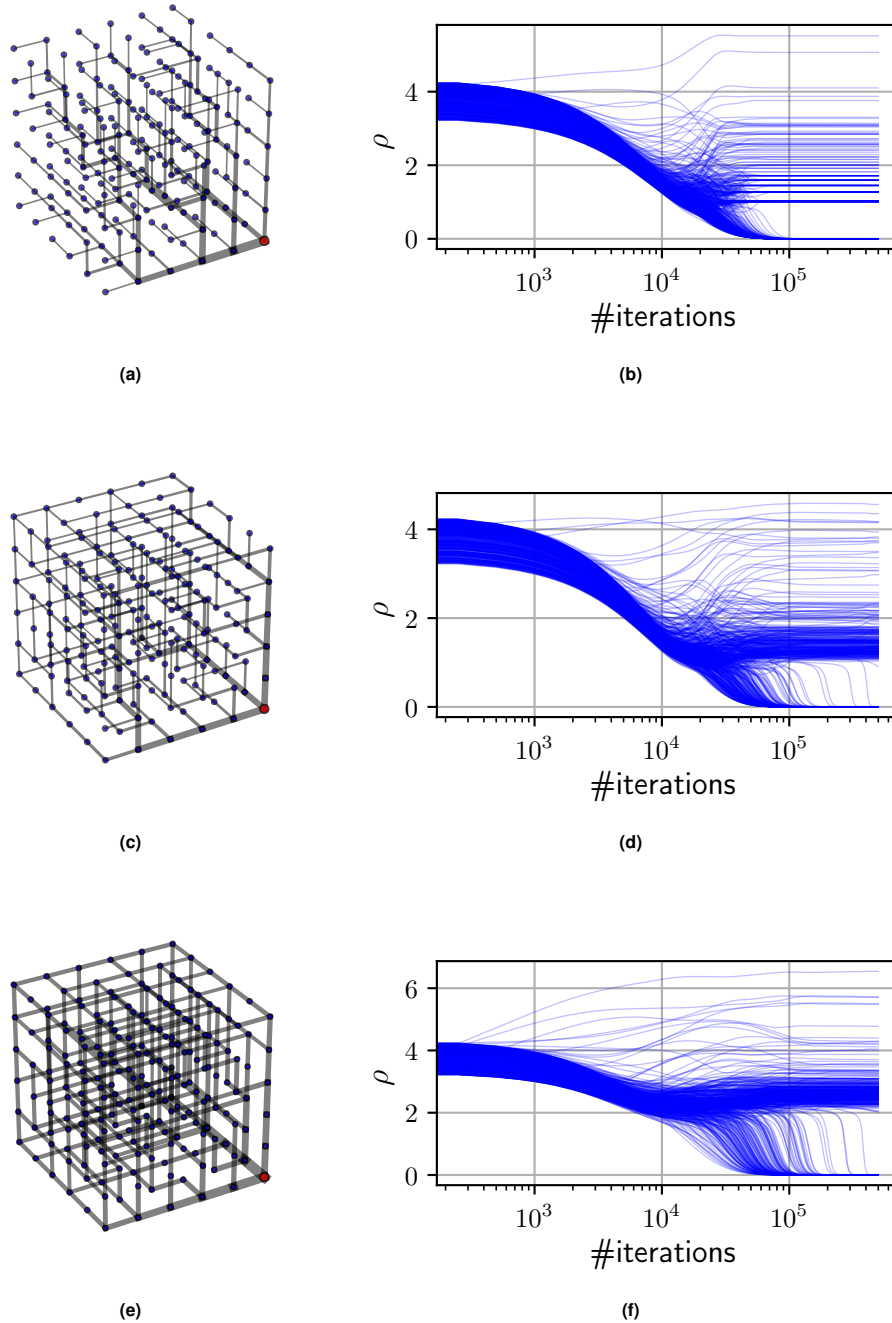


Fig. S2. Adaptation dynamics and pruned network skeletons: (a) + (b) Tree-like configuration for $\lambda_2 = \lambda_3 = 1$. (c) + (d) Onset of reticulation for $\lambda_2 = 1$ and $\lambda_3 = 10$. (e) + (f) Saturation of fluctuation induced loops for $\lambda_2 = 1$ and $\lambda_3 = 1000$. The edge thickness is representative for the relative tube radius ρ . Sinks are marked as blue dots, the source as large red circle.

The actual dynamics and pruned structures are represented for several sample parameters in Fig. S2. Fluctuation induced pruning into spanning trees usually takes place on shorter time-scales than their reticulated pendants and displays less avalanche-like events of a edge radii suddenly collapsing. Nevertheless, there is also a quantitative variation of the final nullity, depending on the total network size, see Figure S3a. How then is the trajectory dependent on the actual system size? An answer could be given by looking into the fluctuation generating machinery which manifests the positive feedback in Eq. (40). Adding up U and V and resorting the terms around

λ_3 , we rewrite $\langle \Delta \Phi_e^2 \rangle$ as,

$$\langle \Delta \Phi_e^2 \rangle = \sum_{jk} \alpha_{jk}^e \mathbf{W}_{jk}(\lambda_3) \quad [41]$$

$$\begin{aligned} \text{with } \mathbf{W}_{jk} &= (1 + \delta_{0j}\delta_{0k} - \delta_{0j} - \delta_{0k}) + \lambda_3 (\delta_{jk} - \delta_{0j}\delta_{0k}) \\ &+ (n-1) \left[(n+1) \delta_{0j}\delta_{0k} - \delta_{0j} - \delta_{0k} \right] \left[1 + \frac{\lambda_3}{n-1} \right] \end{aligned} \quad [42]$$

By introducing further abbreviations to improve readability we rewrite Eq. (41) as,

$$\begin{aligned} \mathbf{W}_{jk} &= \mathbf{w}_{0,jk} + \mathbf{w}_{1,jk}\lambda_3 + \mathbf{w}_{2,jk}h(\lambda_3, n) \quad [43] \\ \text{with } \mathbf{w}_{0,jk} &= (1 + \delta_{0j}\delta_{0k} - \delta_{0j} - \delta_{0k}) \\ \mathbf{w}_{1,jk} &= (\delta_{jk} - \delta_{0j}\delta_{0k}) \\ \mathbf{w}_{2,jk} &= (n-1) \left[(n+1) \delta_{0j}\delta_{0k} - \delta_{0j} - \delta_{0k} \right] \\ h(\lambda_3, n) &= 1 + \frac{\lambda_3}{n-1} \end{aligned}$$

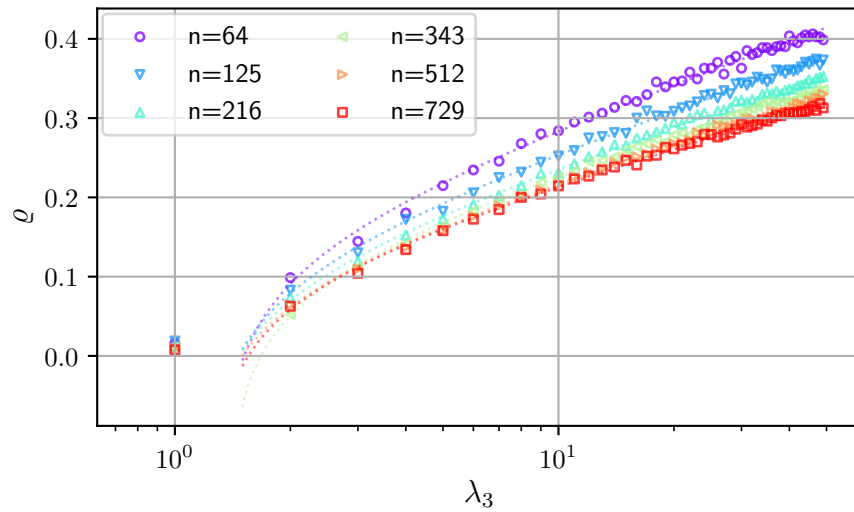
Hence we have $h(\lambda_3, n) \rightarrow 1$, for large networks with small fluctuations $\lambda_3 \ll n$, so the solution in Eq. (43) becomes,

$$\mathbf{W}_{jk} \approx (\mathbf{w}_{0,jk} + \mathbf{w}_{2,jk}) + \mathbf{w}_{1,jk}\lambda_3 \quad [44]$$

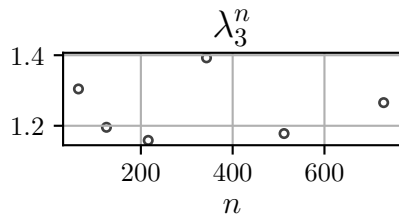
This impact on the (positive) feedback terms suggest a size dependent change in the overall network structure. Though we can't exclude the possibility of other finite size effects, such as the ratio of surface (nodes with a degree smaller than the maximal possible for the lattice) to volume nodes (nodes with maximum degree). We can observe the transition to follow a logarithmic relation for any network size (node number n),

$$\varrho_n(\lambda_3) = a_n \cdot \lg(\lambda_3 - \lambda_3^n) + b_n \quad [45]$$

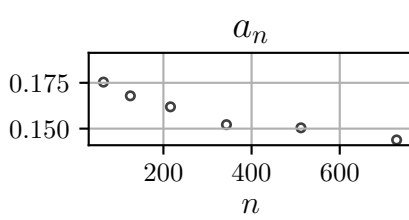
¹⁷ From fitting the trajectories in [S3a](#) one can quantitatively see that the transition curves converge with increasing n at given λ_3 ,
¹⁸ suggesting our approximation to be a plausible cause.



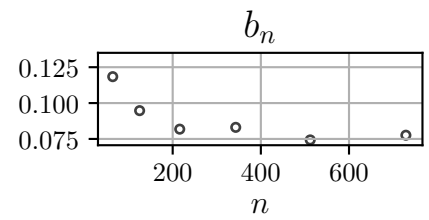
(a)



(b)



(c)



(d)

Fig. S3. Size dependency for nullity transition in cubic lattice: (a) Different network sizes (amount of nodes) and logarithmic fits for $\lambda_2 = 1$. (b) - (d) Size dependencies of the fit parameters λ_3^n , a_n and b_n .

20 In the following we collected the entirety of numeric results for both networks spanning our system, including an overview of
 21 the respective adaptation dynamics during the the optimization and plots of pruned network skeletons starting from cubic,
 22 diamond and Laves graph topologies. We begin with a commented section of the 'dual' cubic graphs. Further we find
 23 qualitative similar results for other graph topologies such as the 'dual' diamond graphs and the 'dual' Laves graphs. The edge
 24 affiliation definition from cubic networks will be redefined at this point: Instead of affiliating edges penetrating faces we define
 25 distance criterion stating that edges should have a distance d for given network topology to be affiliated with each other, see
 table [S1](#).

Topology	distance (in units of the constructed graph's node positions)	max. number of affiliations per edge
dual cubic	0.5	4
dual diamond	$\sqrt{2}$	6
dual Laves	$\sqrt{14}$	8

Table S1. Specifics for intertwined graph topologies of the triply periodic surfaces P, D and G

26

27 In Figure [S5](#) we present the nullity transition for the intertwined cubic networks, displaying yet again the retardation of the
 28 transitions onset for increasing coupling λ_1 . The dual cubic structure was generated by first repeating a unit cell (consisting of
 29 points $(0, 0, 0)$, $(0, 0, 1)$, $(1, 0, 0)$, $(0, 1, 0)$, $(1, 1, 1)$, $(1, 0, 1)$, $(0, 1, 1)$, $(1, 1, 0)$, connecting those pairs of relative distance $\delta = 1$)
 30 periodically with the three translation vectors $\mathbf{a} = i * (1, 0, 0)$, $\mathbf{b} = j * (0, 1, 0)$, $\mathbf{c} = k * (0, 0, 1)$ with $i, j, k \in \mathbb{Z}$. The second
 31 network is acquired by copying the first structure and shifting it by $\mathbf{t} = (0.5, 0.5, 0.5)$.

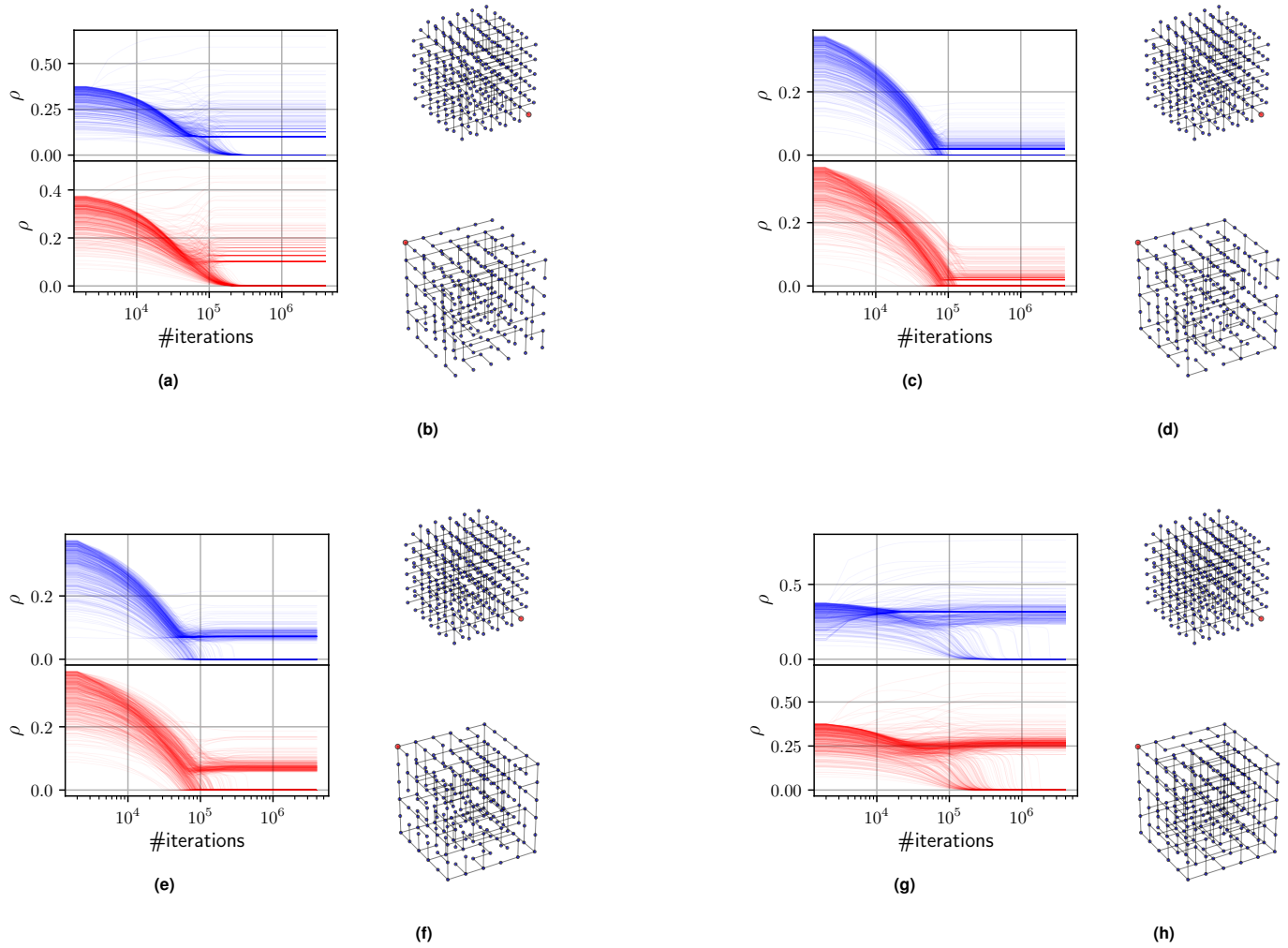


Fig. S4. Adaptation Dynamics for a 'dual' cubic lattice system and pruned network skeletons. The edge thickness is representative for the relative tube radius ρ . (a) + (b) $\lambda_1 = 1, \lambda_3 = 0.1$ (c) + (d) $\lambda_1 = 10^8, \lambda_3 = 0.1$ (e) + (f) $\lambda_1 = 10^8, \lambda_3 = 10^3$ (g) + (h) $\lambda_1 = 1, \lambda_3 = 10^3$

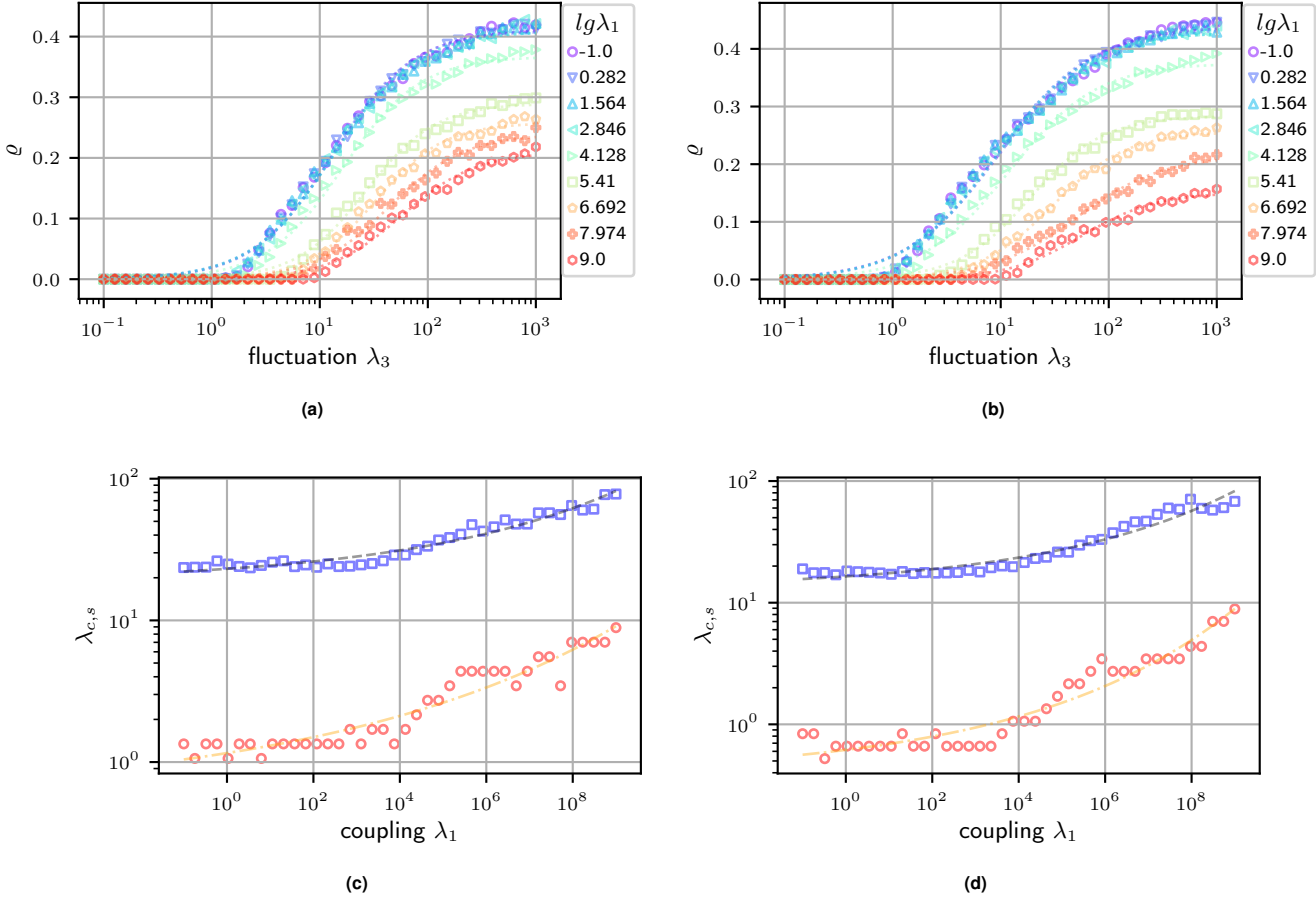


Fig. S5. Numeric results and analysis of for a 'dual' cubic lattice system: (c) + (d) Continuous, logarithmic nullity transition in dependency for various coupling λ_1 . Increasing coupling breaks down fluctuation induced nullity. (c) + (d) Saturation (blue, squares) and critical values (red circles) in dependency of coupling λ_1 .

32 Phenomenologically, the transition resembles an asymmetrical sigmoidal for $\lambda_3 > \lambda_c$, whose saturation value, steepness and
 33 x-offset are functions of λ_1 . Note that, though qualitatively similar, the curves development for increasing λ_1 is different in the
 34 two networks. In particular we observe a significant change of the saturation onset in the second network, see Figure S5c, S5d.
 35 Next we have listed the systematic λ_1 , λ_3 of the final stationary state after pruning. In Figure S6a, S6b we present the nullity
 36 state diagrams as well as the respective outline of their transition zones: first spanning trees, second the onset of redundancy
 37 and third the onset of saturation. The colored, dashed boundaries of these zones represent the curves' fits from Figure S5c and
 38 S5c. In Figure S6c, S6d we show dissipation diagrams, presenting the the systems power dissipation $D = \sum_e \kappa_{ee} \langle \Delta \Phi_e^2 \rangle$ for
 39 each network. Note that the systems dissipation is not significantly increased by an increase of the coupling until extreme
 40 values for λ_1 are reached. In Figure S6e, S6f we show the networks volume calculated as $V = \sum_e \rho_e^2$ (vessel segments are
 41 modelled as cylindrical tubes). We observe here that the tube system collapses for $\lambda_1 > 10^5$ in opposition to the fluctuation
 42 induced increase of the systems volume. In Figure S10 we present the numeric results for the systems radii dynamics and plots
 43 of the pruned networks for various parameter combinations. An increase in $\lambda_1 = \frac{b(\varepsilon-1)}{\pi l \eta L^{\varepsilon+1}} \left(\frac{\mu}{L^3} \right)^{-2}$ is decreasing the final radius
 44 size ρ_e , as it incorporates not only the strength of the repulsive potential but can also be seen as an increase off the systems
 45 density by bringing the edges closer to each other.

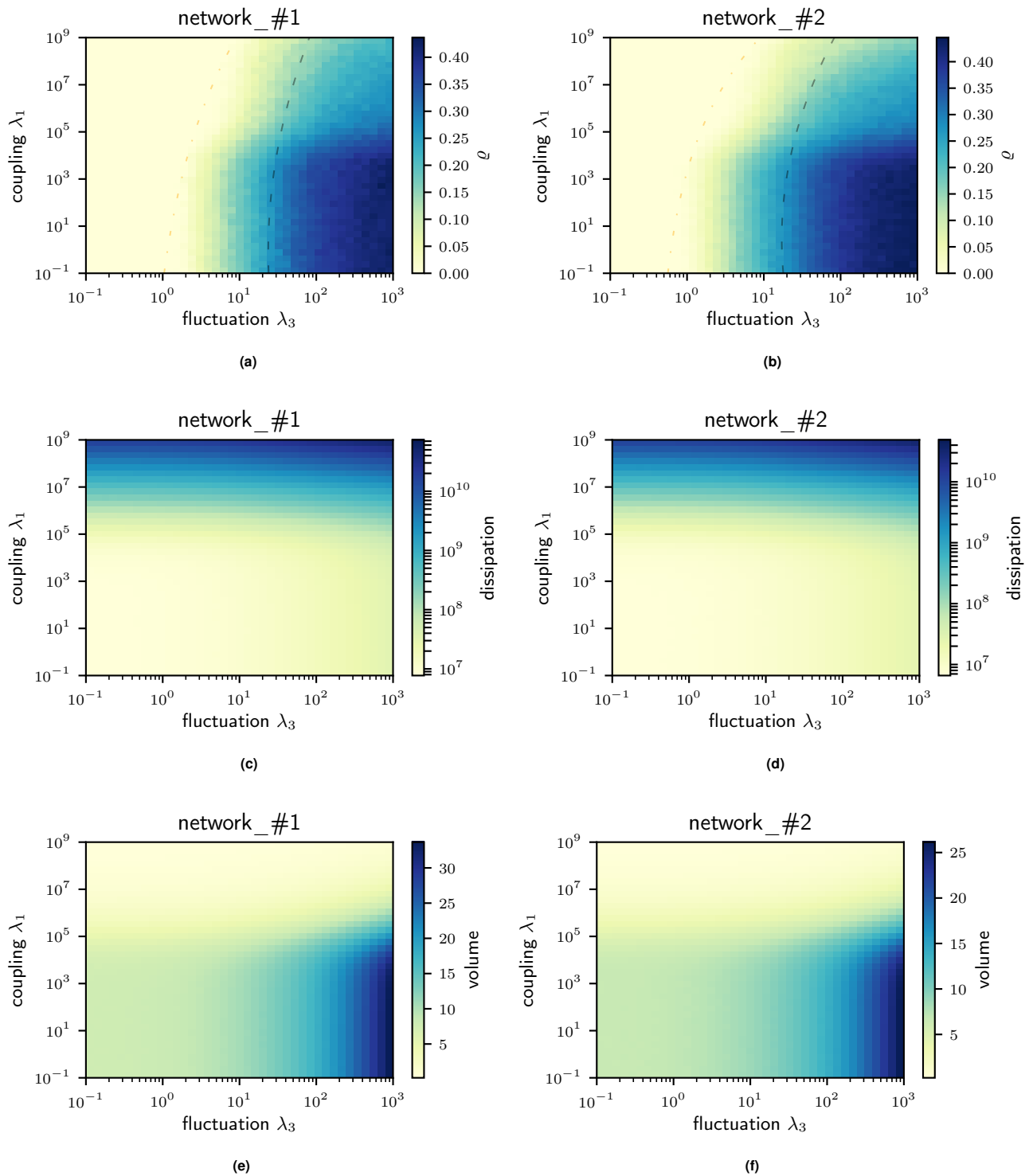


Fig. S6. Numeric results and analysis for a 'dual' cubic lattice system: (a) + (b) Nullity ρ state diagrams with borders of the transition zones plotted as dashed lines(red = onset of nullity transition, black = onset of saturation) (c) + (d) Dissipation diagrams, coupling λ_1 and fluctuation λ_3 are not majorly affecting the systems dissipation (e) + (f) Volume diagrams, we observe an increase of V for increased λ_3 , a collapse is occurring for increased λ_1 .

46 The next segment will contain the gathered results for dual diamond structures where we see the results to be very similar to
 47 the cubic structure. The dual structure was generated by first repeating a unit cell (consisting of points $(0, 0, 0), (0.5, 0.5, 0.5),$
 48 $(1, 0, 1), (0, 1, 1), (1, 1, 0)$, connecting those pairs of relative distance $\delta = \sqrt{3}/2$) periodically with the three translation vectors
 49 $\mathbf{a} = i * (1, 0, 0), \mathbf{b} = j * (0, 1, 0), \mathbf{c} = k * (0, 0, 1)$ with $i, j, k \in \mathbb{Z}$ and $(i + j + k) \bmod 2 = 0$. The second network is acquired by
 50 copying the first structure and shifting it by $\mathbf{t} = (1, 1, 1)$.

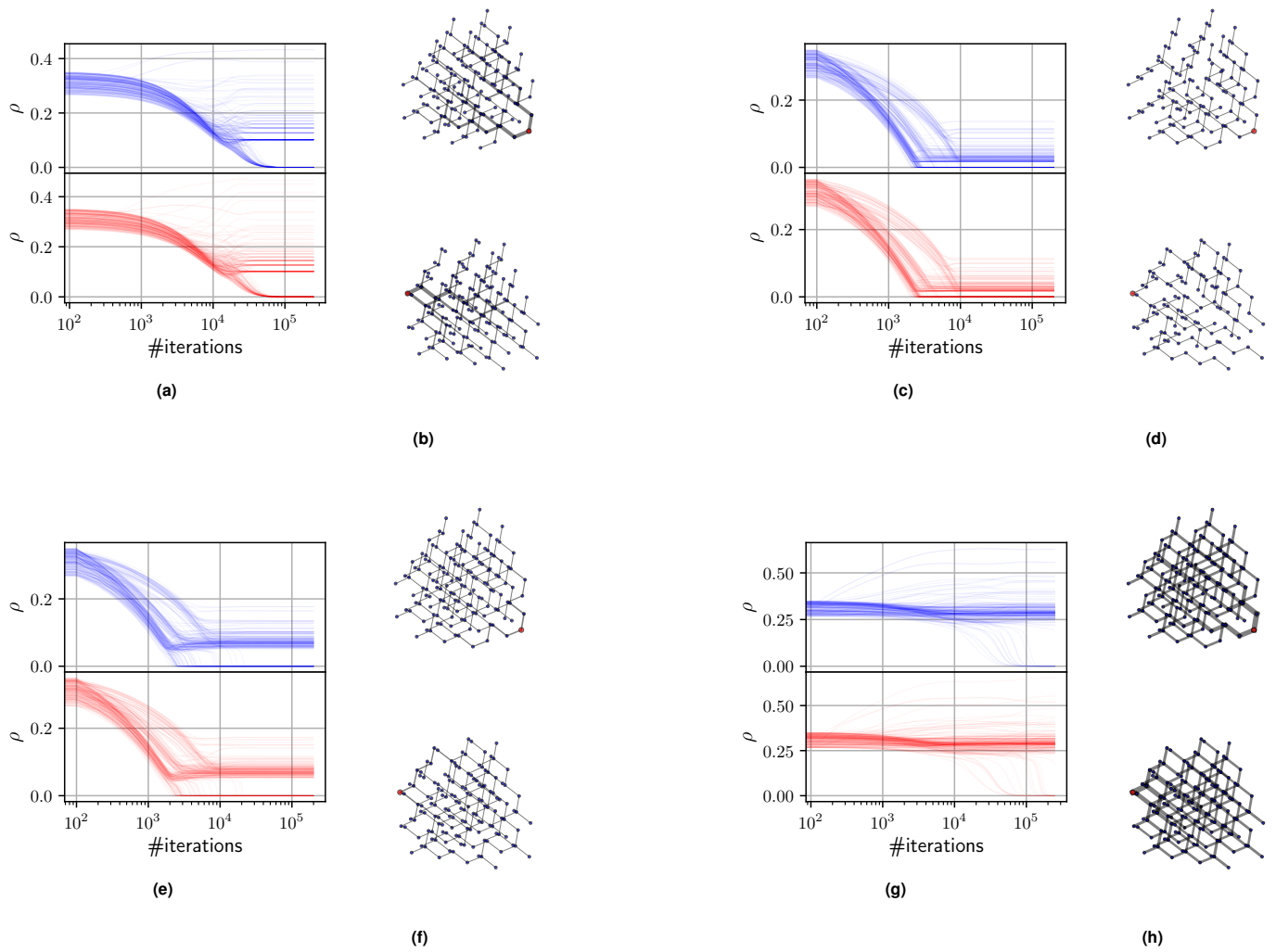
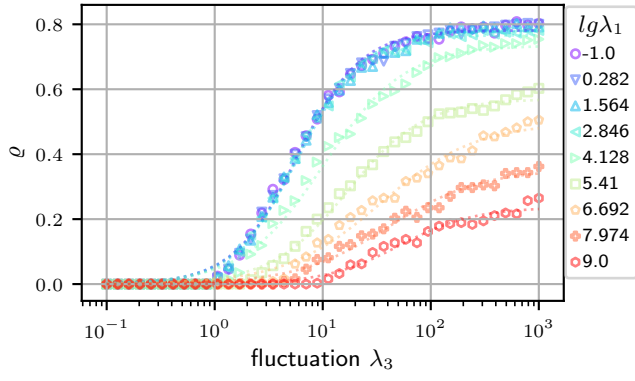
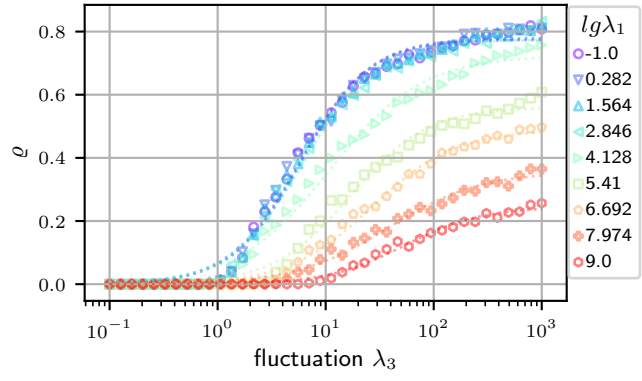


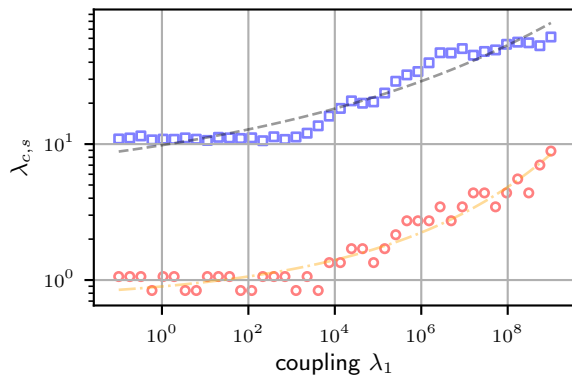
Fig. S7. Adaptation Dynamics for a 'dual' diamond graph system and pruned network skeletons. The edge thickness is representative for the relative tube radius ρ . (a) + (b) $\lambda_1 = 1, \lambda_3 = 0.1$ (c) + (d) $\lambda_1 = 10^8, \lambda_3 = 0.1$ (e) + (f) $\lambda_1 = 10^8, \lambda_3 = 10^3$ (g) + (h) $\lambda_1 = 1, \lambda_3 = 10^3$



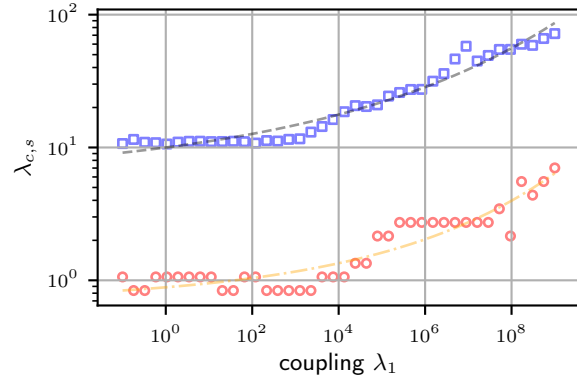
(a)



(b)



(c)



(d)

Fig. S8. Numeric results and analysis for a 'dual' diamond graph system: (c) + (d) Continuous, logarithmic nullity transition in dependency for various coupling λ_1 . Increasing coupling breaks down fluctuation induced nullity. (c) + (d) Saturation (blue, squares) and critical values (red circles) in dependency of coupling λ_1 .

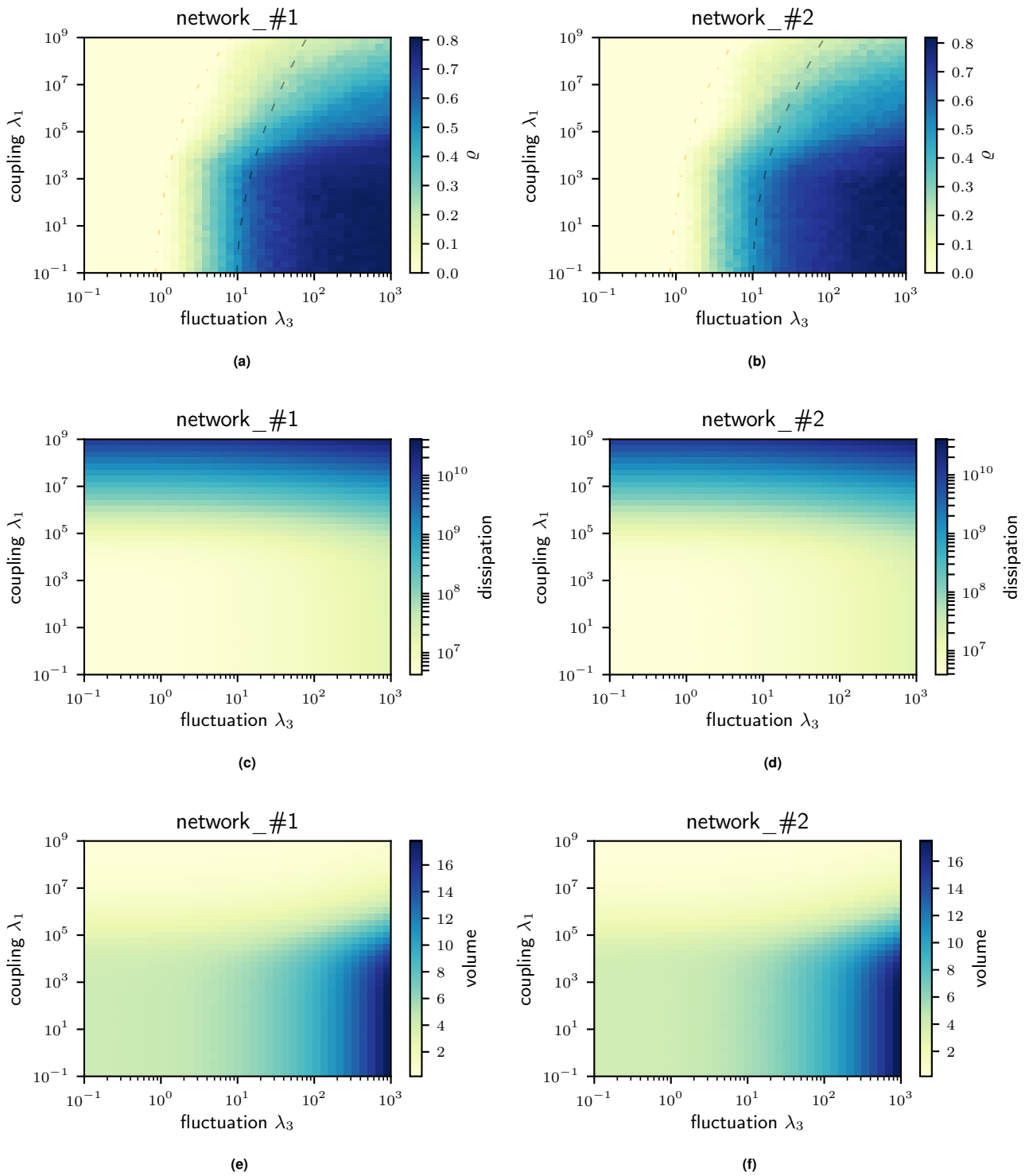


Fig. S9. Numeric results and analysis for a 'dual' diamond graph system: (a) + (b) Nullity ρ state diagrams with borders of the transition zones plotted as dashed lines (red = onset of nullity transition, black = onset of saturation) (c) + (d) Dissipation diagrams, coupling λ_1 and fluctuation λ_3 are not majorly affecting the systems dissipation (e) + (f) Volume diagrams, we observe an increase of V for increased λ_3 , a collapse is occurring for increased λ_1 .

51 The next segment will contain the gathered results for dual Laves structures where we see the results as well to be very similar
52 to the cubic structure. The dual structure was generated by first repeating a unit cell (consisting of points $(0, 0, 0), (1, 1, 0),$
53 $(1, 2, 1), (0, 3, 1), (2, 2, 2), (3, 3, 2), (3, 0, 3), (2, 1, 3)$, connecting those pairs of relative distance $\delta = \sqrt{2}$) periodically with the
54 three translation vectors $\mathbf{a} = i * (4, 0, 0), \mathbf{b} = j * (0, 4, 0), \mathbf{c} = k * (0, 0, 4)$ with $i, j, k \in \mathbb{Z}$. The second network is acquired
55 mirroring in order to create the opposing chirality of the first structure, i.e. $\mathbf{a} \rightarrow -\mathbf{a}$, and shifting it by $\mathbf{t} = (3, 2, 0)$.

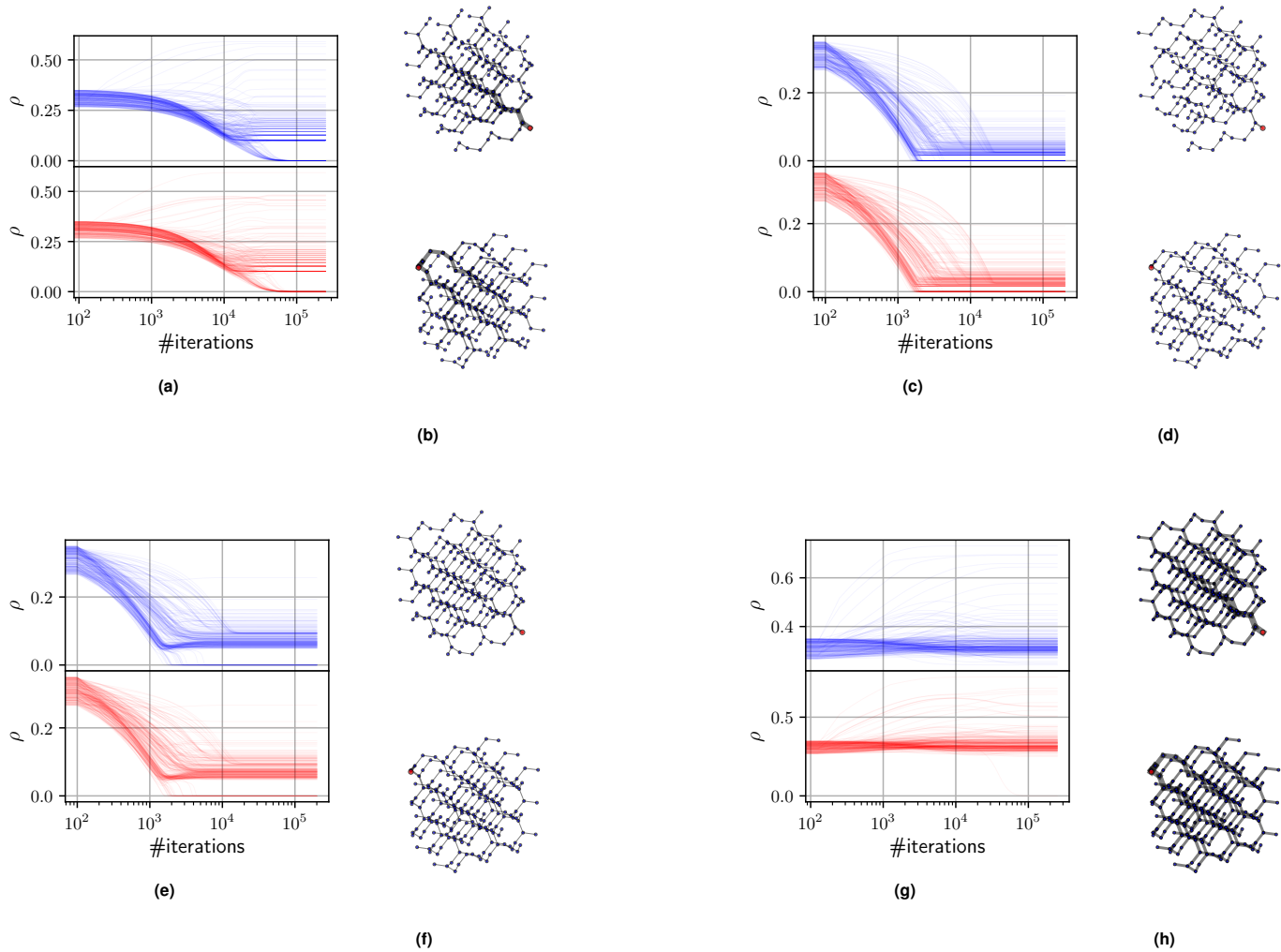
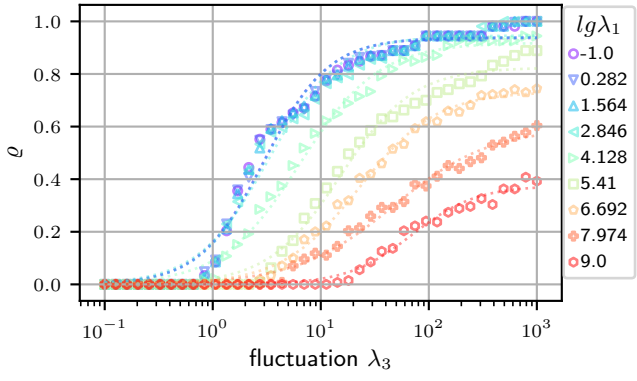
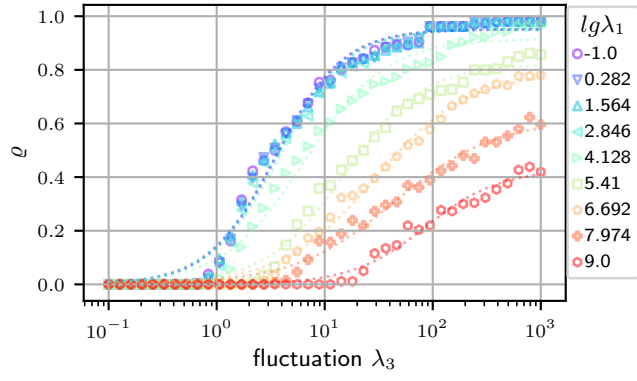


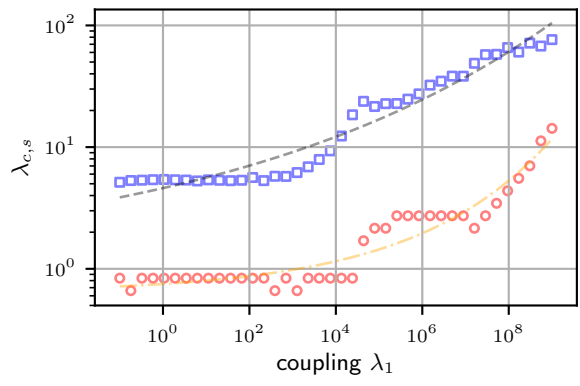
Fig. S10. Adaptation Dynamics for a 'dual' Laves graph system and pruned network skeletons. The edge thickness is representative for the relative tube radius ρ . (a) + (b) $\lambda_1 = 1, \lambda_3 = 0.1$ (c) + (d) $\lambda_1 = 10^8, \lambda_3 = 0.1$ (e) + (f) $\lambda_1 = 10^8, \lambda_3 = 10^3$ (g) + (h) $\lambda_1 = 1, \lambda_3 = 10^3$



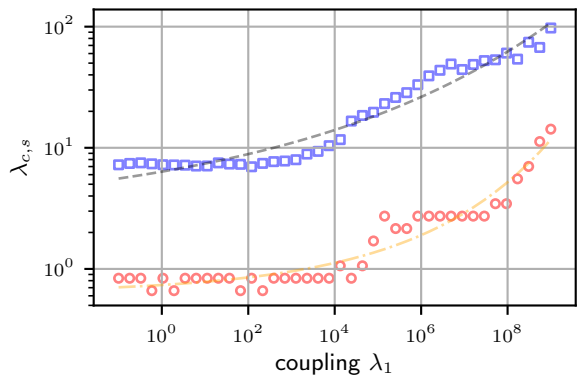
(a)



(b)



(c)



(d)

Fig. S11. Numeric results and analysis for a 'dual' Laves graph system: (c) + (d) Continuous, logarithmic nullity transition in dependency for various coupling λ_1 . Increasing coupling breaks down fluctuation induced nullity. (c) + (d) Saturation (blue, squares) and critical values (red circles) in dependency of coupling λ_1 .

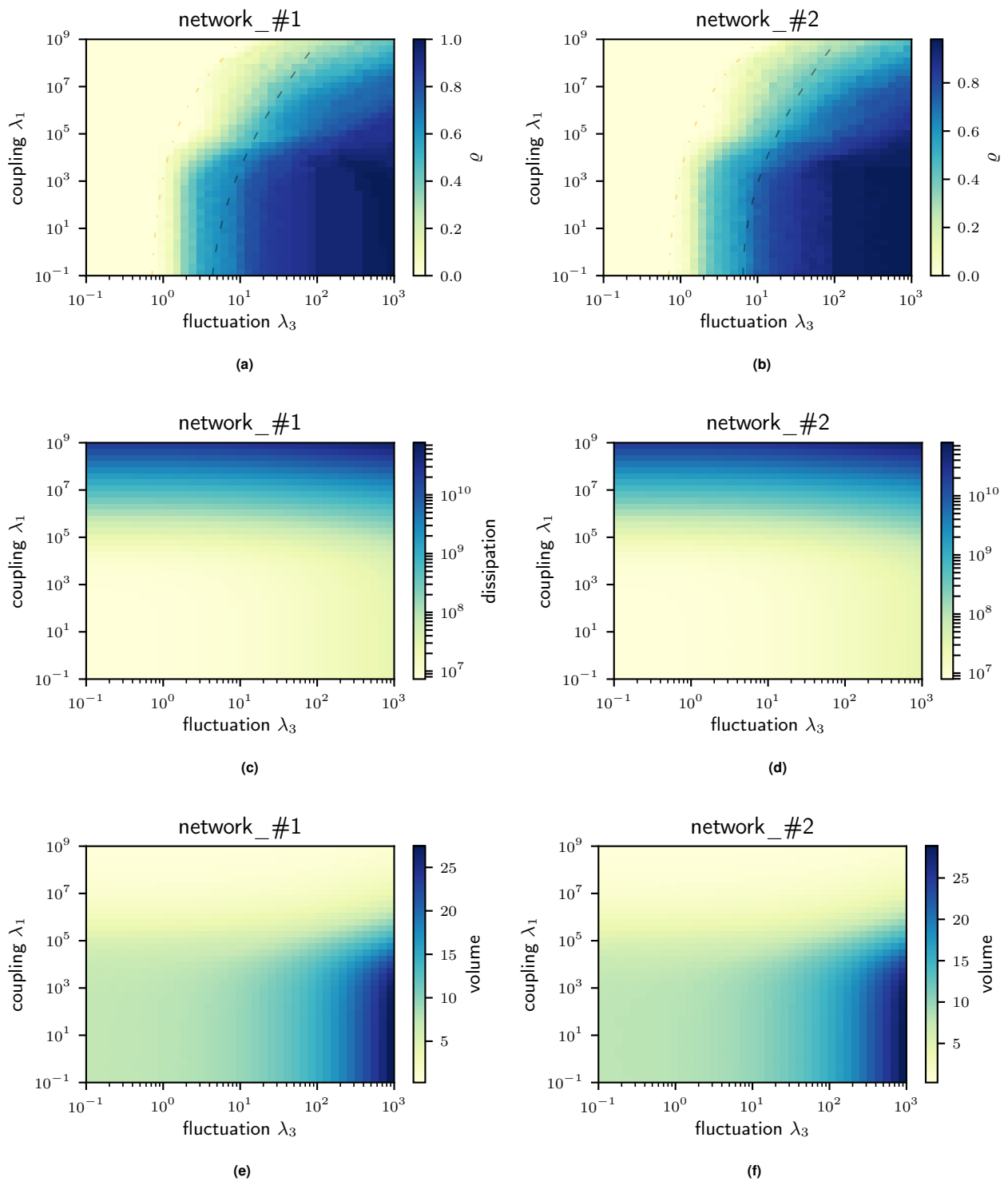


Fig. S12. Numeric results and analysis for a 'dual' Laves graph system: (a) + (b) Nullity ρ state diagrams with borders of the transition zones plotted as dashed lines (red = onset of nullity transition, black = onset of saturation) (c) + (d) Dissipation diagrams, coupling λ_1 and fluctuation λ_3 are not majorly affecting the systems dissipation (e) + (f) Volume diagrams, we observe an increase of V for increased λ_3 , a collapse is occurring for increased λ_1 .

This section centers around the scaling laws resulting from the formalism. One can show that introducing fluctuations and coupling alter the classical form of Murray's law $\rho_0^3 = \rho_1^3 + \rho_2^3$ in the following way: Given the Kirchhoff current law we and rewriting it via Ohm's law into a reduced form, we get for all nodes i and reference flow μ ,

$$\sum_e B_{ie} f_e = s_i \Leftrightarrow \sum_e B_{ie} \rho_e^4 \Delta \Phi_e = s_i / \mu \quad [46]$$

Taking the average over all pressure configurations between two adaptation events we get

$$\sum_e B_{ie} \rho_e^4 \langle \Delta \Phi_e \rangle = \langle s_i \rangle / \mu \Leftrightarrow \sum_e \Theta_{ie} \rho_e^4 |\langle \Delta \Phi_e \rangle| = \langle s_i \rangle / \mu \quad [47]$$

with $\Theta_{ie} = \begin{cases} \pm 1 \\ 0 \end{cases}$ distinguishing between in- and outgoing flows on the relevant edges, see Figure S13. In order to acquire the cubic form we substitute one multiplicand ρ_e with the result of the stationary states equation,

$$\partial_h \rho_e = 0 \Rightarrow (\rho_e^2 \langle \Delta \Phi_e^2 \rangle - \lambda_2) \rho_e - \lambda_1 \sum_{ee'} F_{ee'} \Delta \rho_{ee'}^{-\epsilon} = 0 \quad [48]$$

$$\Leftrightarrow \rho_e = \frac{\sqrt{\lambda_2 + \lambda_1 \rho_e^{-1} \sum_{ee'} F_{ee'} \Delta \rho_{ee'}^{-\epsilon}}}{\sqrt{\langle \Delta \Phi_e^2 \rangle}} \quad [49]$$

Plugging Eq. (49) into Eq. (47) and rewriting $|\langle \Delta \Phi_{e'} \rangle| = \sqrt{\langle \Delta \Phi_{e'}^2 \rangle}$, $g_e(\epsilon) = \rho_e^{-1} \sum_{ee'} F_{ee'} \Delta \rho_{ee'}^{-\epsilon}$ we get,

$$\sum_e \Theta_{ie} \sqrt{(\lambda_2 + \lambda_1 g_e(\epsilon)) \frac{\langle \Delta \Phi_e \rangle^2}{\langle \Delta \Phi_e^2 \rangle}} \rho_e^3 = \langle s_i \rangle / \mu \quad [50]$$

We know from section 2 that $\langle \Delta p_e^2 \rangle = \sum_{jk} \mathbf{A}_{jk}^e \langle s_j s_k \rangle$ and may also deduce $\langle \Delta p_e \rangle^2 = \sum_{jk} \mathbf{A}_{jk}^e \langle s_j \rangle \langle s_k \rangle$. This enables us to calculate the ratio via the covariance,

$$\frac{\langle \Delta p_e^2 \rangle}{\langle \Delta p_e \rangle^2} = \frac{\sum_{jk} \mathbf{A}_{jk}^e \langle s_j s_k \rangle}{\sum_{jk} \mathbf{A}_{jk}^e \langle s_j \rangle \langle s_k \rangle} \quad [51]$$

$$= \frac{\sum_{jk} \mathbf{A}_{jk}^e [\langle s_j \rangle \langle s_k \rangle + \langle (s_j - \langle s_j \rangle) (s_k - \langle s_k \rangle) \rangle]}{\sum_{jk} \mathbf{A}_{jk}^e \langle s_j \rangle \langle s_k \rangle} \quad [52]$$

$$= 1 + \frac{\sum_{jk} \mathbf{A}_{jk}^e \langle (s_j - \langle s_j \rangle) (s_k - \langle s_k \rangle) \rangle}{\sum_{jk} \mathbf{A}_{jk}^e \langle s_j \rangle \langle s_k \rangle} \quad [53]$$

Substituting this into Eq. (50) and having $\frac{\langle \Delta p_e^2 \rangle}{\langle \Delta p_e \rangle^2} = \frac{\langle \Delta \Phi_e^2 \rangle}{\langle \Delta \Phi_e \rangle^2}$, $H_e = \frac{\sum_{jk} \mathbf{A}_{jk}^e \langle (s_j - \langle s_j \rangle) (s_k - \langle s_k \rangle) \rangle}{\sum_{jk} \mathbf{A}_{jk}^e \langle s_j \rangle \langle s_k \rangle}$ we get,

$$\sum_e a_e \rho_e^3 = \langle s_i \rangle / \mu \quad [54]$$

$$\text{setting } a_e = \Theta_{ie} \sqrt{\frac{\lambda_2 + \lambda_1 g_e(\epsilon)}{1 + H_e}} \quad [55]$$

One may simplify this complex by considering the following: First, let's assume that we have for all sink nodes $\langle s_i \rangle = \mu$ and secondly to have uncorrelated, identically distributed sinks as in section 2, Eq. (32). This leads to the equation presented in the paper's main body,

$$\sum_e a_e \rho_e^3 = 1 \quad [56]$$

$$\text{with } a_e = \Theta_{ie} \sqrt{\frac{\lambda_2 + \lambda_1 g_e(\epsilon)}{1 + \lambda_3 h_e}} \quad [57]$$

$$\text{and } h_e = \frac{\sum_{jk} \mathbf{A}_{jk}^e \mathbf{V}_{jk}}{\sum_{jk} \mathbf{A}_{jk}^e \mathbf{U}_{jk}} \quad [58]$$

The structure of Eq. (58) is unchanged by introducing multiple sources (clones) into the system, with exception for the specific entries of \mathbf{U} , \mathbf{V} , see Eq. (36). For experimental validation of Eq. (56) it will be necessary to know the networks vessel radii as

well as the sink/source pattern (although it may be sufficient to know where the system's source is and to consider every other node as sink). One should consider simple Y-branchings of low sink/source value (points of neglectable secreting/leakage) such that $|a_e \rho_e^3| \gg 1$, further setting the index for the largest vessel to zero (and accordingly increasing for the other vessel pieces at the branching) may write,

$$a_0 \rho_0^3 = a_1 \rho_1^3 + a_2 \rho_2^3 \quad [59]$$

57 Doing so we can demonstrate the quality of this procedure for sink-source conditions, see Figures S17, S18, S19 showing that
 58 increasing number of cloned sinks does not alter the quality of the estimation. We would like note though that the estimation
 59 gets considerably worse when encountering a parameter regime which impose neglectable interactions such as $\lambda_1 < 10^3$ or
 60 $\lambda_3 < 10^{-1}$.

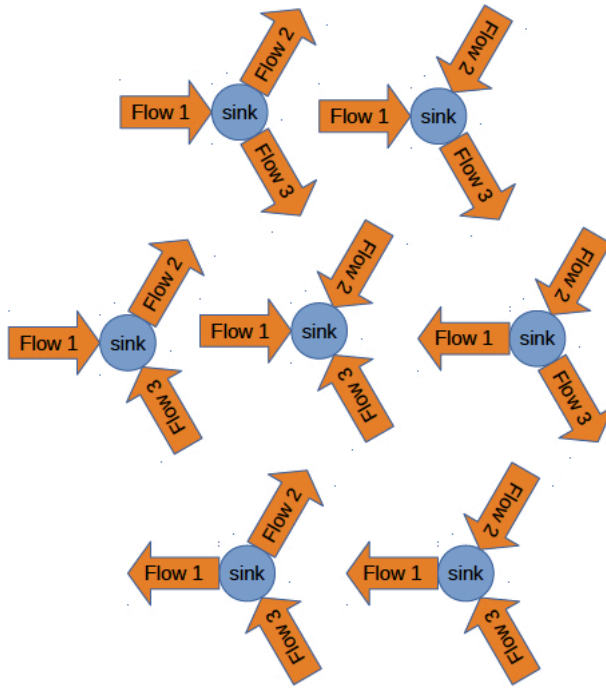


Fig. S13. Scheme of identifying different flow combinations at a sink determining the respective sign of Θ_{ie} , here shown for Y-branching point. Let's identify the sink as $i = 0$ and the respective flow carrying edges as $e \in \{1, 2, 3\}$ and define a triplet $\Theta = (\Theta_{01}, \Theta_{02}, \Theta_{03})$. Reading from left to right we have in the top diagram: $\Theta = (1, -1, -1)$, $\Theta = (1, 1, -1)$ Middle diagram: $\Theta = (1, -1, 1)$, $\Theta = (1, 1, 1)$, $\Theta = (-1, 1, -1)$ Bottom diagram: $\Theta = (-1, -1, 1)$, $\Theta = (-1, 1, 1)$

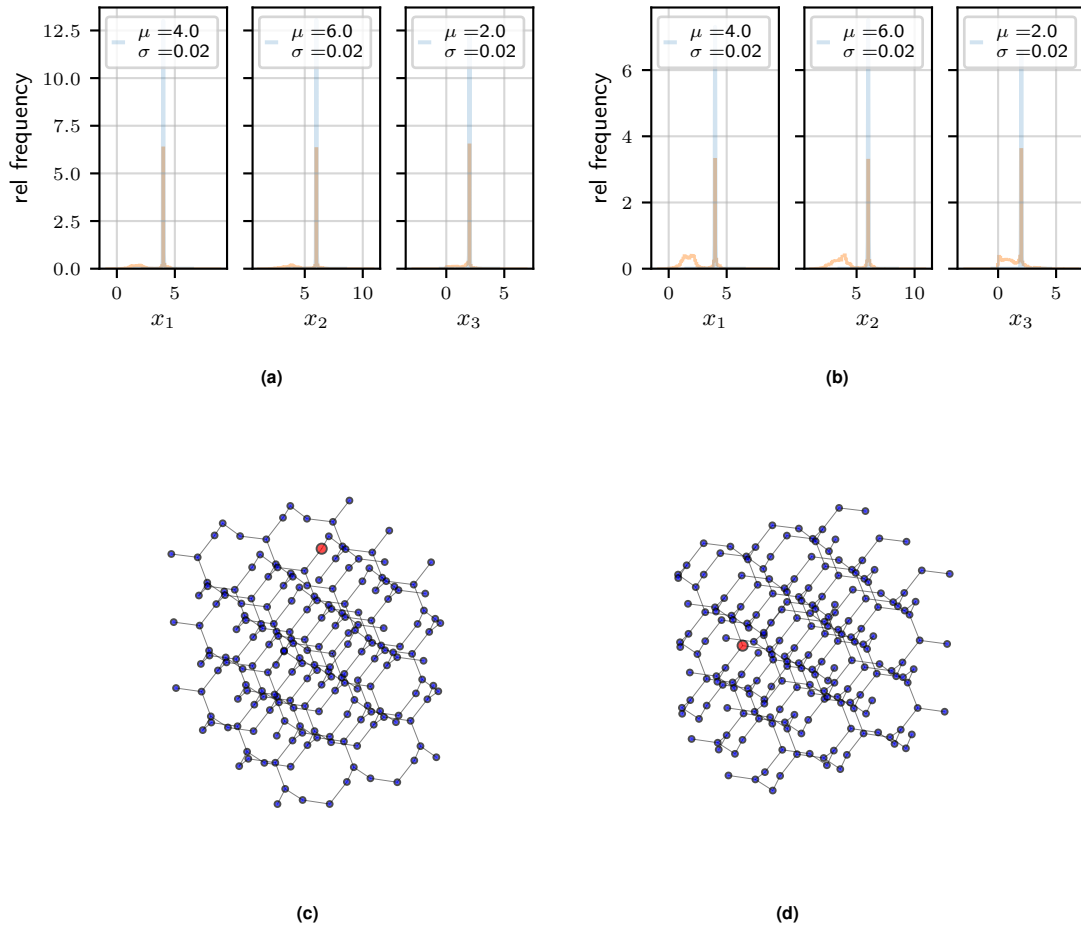


Fig. S14. (a) + (b) Parameters Histograms and fits $\mathcal{N}(\mu, \sigma)$ presenting the estimated simulation parameters λ_i for both networks in an ideal Kirchhoff network, dual Laves-Graph topology, single source-multi-sink system, rescaled axis is $x_i = \log_{10} \lambda_i$, the system was initialised symmetrically with $x_1 = 4$, $x_2 = 6$ and $x_3 = 2$ (c) + (d) Network plots of the respective reticulated networks.

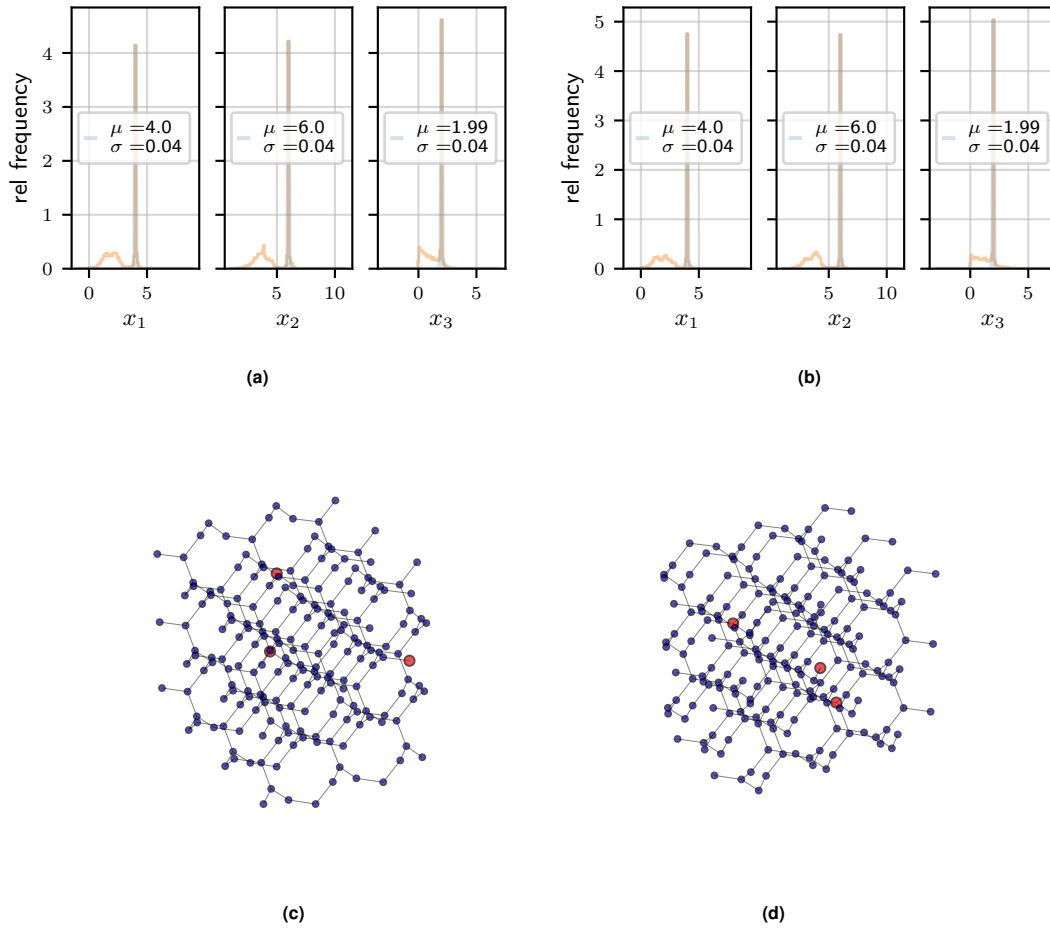


Fig. S15. (a) + (b) Parameters Histograms and fits $\aleph(\mu, \sigma)$ presenting the estimated simulation parameters λ_i for both networks in an ideal Kirchhoff network, dual Laves-Graph topology, multi-source-multi-sink system (three sources), rescaled axis is $x_i = \log_{10} \lambda_i$, the system was initialised symmetrically with $x_1 = 4$, $x_2 = 6$ and $x_3 = 2$ (c) + (d) Network plots of the respective reticulated networks, showing the three initialized 'cloned' sources in red.

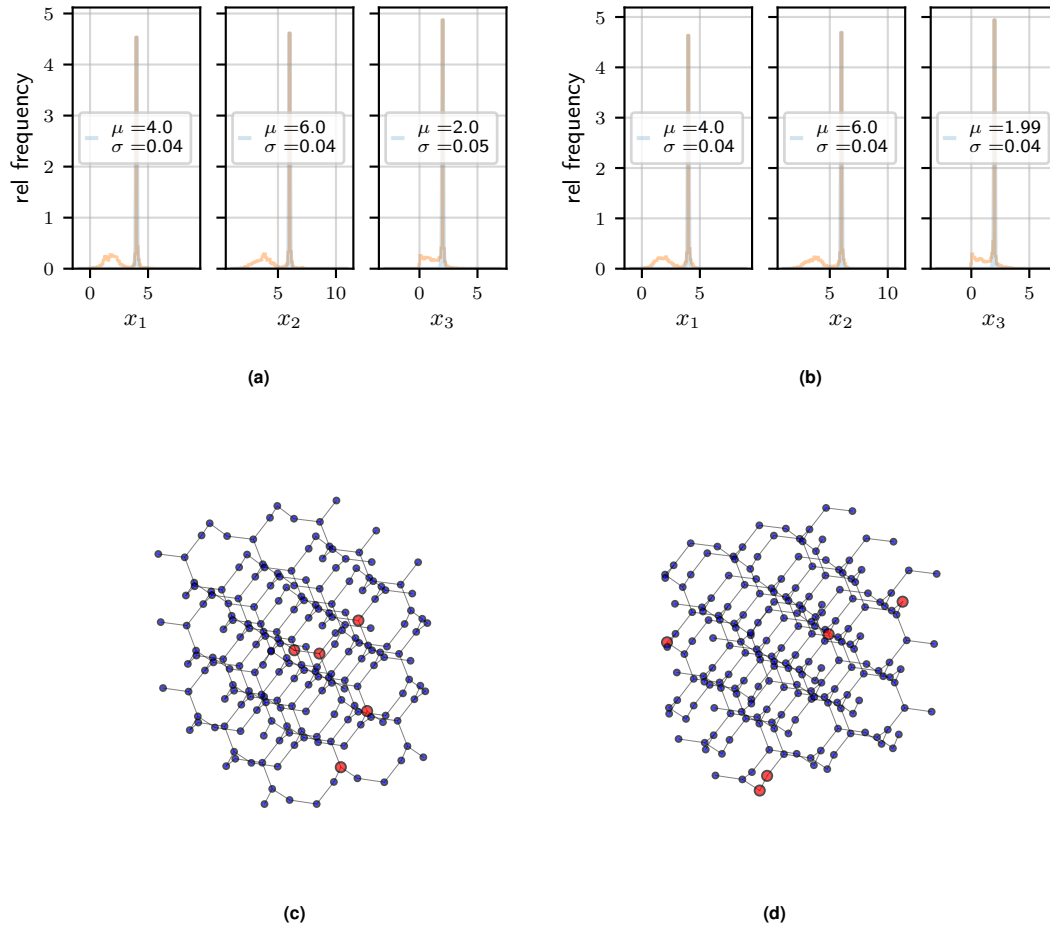


Fig. S16. (a) + (b) Parameters Histograms and fits $\mathcal{N}(\mu, \sigma)$ presenting the estimated simulation parameters λ_i for both networks in an ideal Kirchhoff network, dual Laves-Graph topology, multi-source-multi-sink system (five sources), rescaled axis is $x_i = \log_{10}\lambda_i$, the system was initialised symmetrically with $x_1 = 4$, $x_2 = 6$ and $x_3 = 2$ (c) + (d) Network plots of the respective reticulated networks, showing the five initialized 'cloned' sources in red.

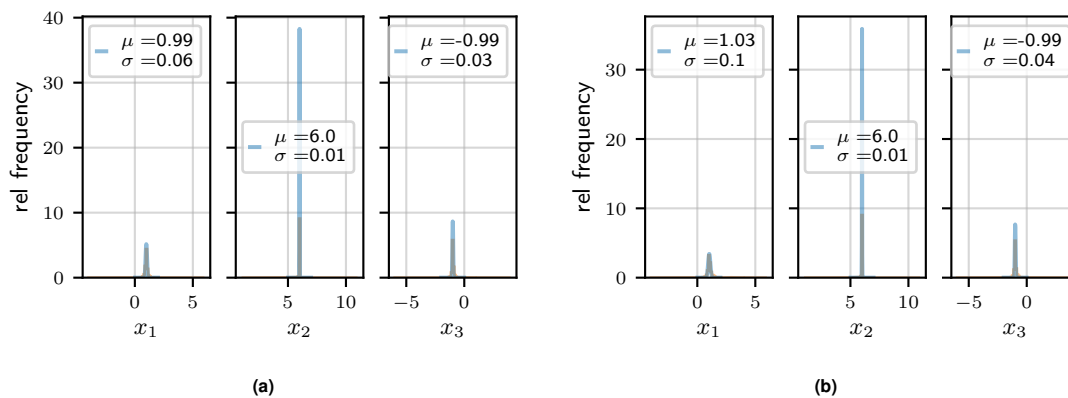


Fig. S17. (a) + (b) Parameters Histograms and fits $\mathcal{N}(\mu, \sigma)$ presenting the estimated simulation parameters λ_i for both networks in an ideal Kirchhoff network, dual Laves-Graph topology, single source-multi-sink system, rescaled axis is $x_i = \log_{10}\lambda_i$, the system was initialised symmetrically with $x_1 = 1$, $x_2 = 6$ and $x_3 = -1$

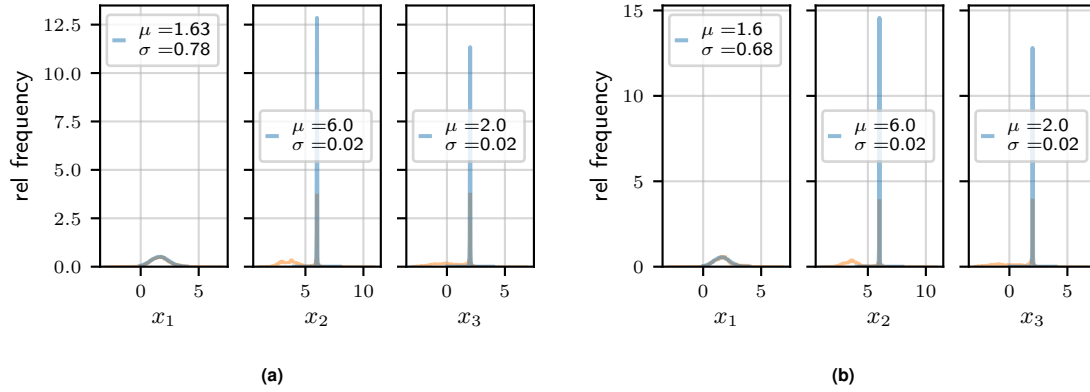


Fig. S18. (a) + (b) Parameters Histograms and fits $\mathcal{N}(\mu, \sigma)$ presenting the estimated simulation parameters λ_i for both networks in an ideal Kirchhoff network, dual Laves-Graph topology, multi-source-multi-sink system, rescaled axis is $x_i = \log_{10} \lambda_i$, the system was initialised symmetrically with $x_1 = 2$, $x_2 = 6$ and $x_3 = 2$

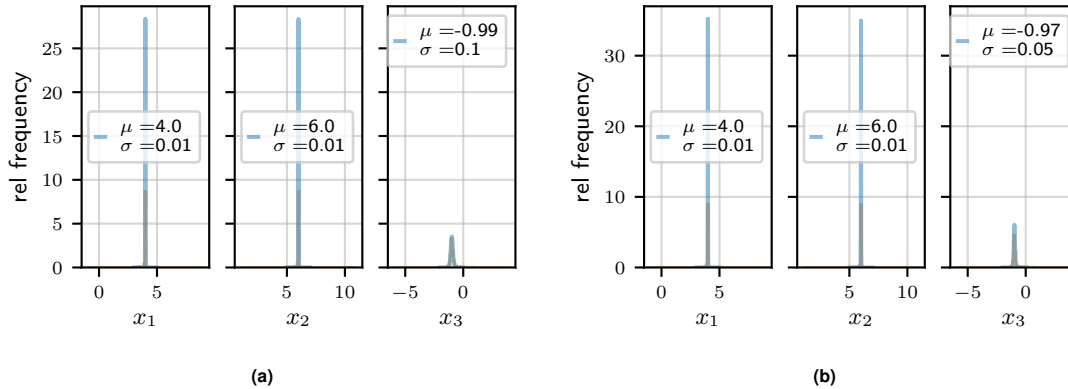
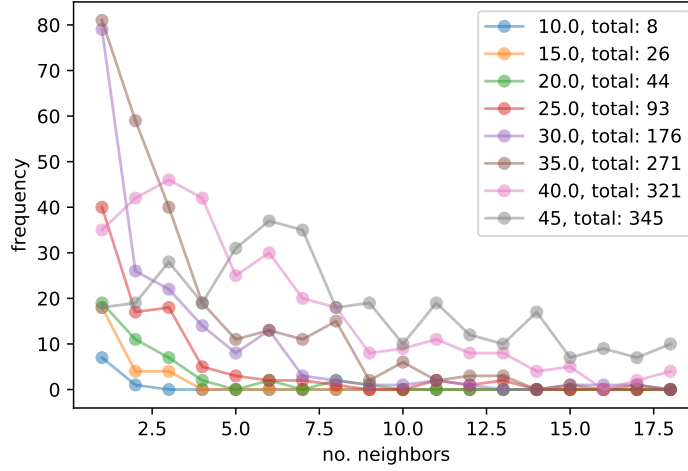
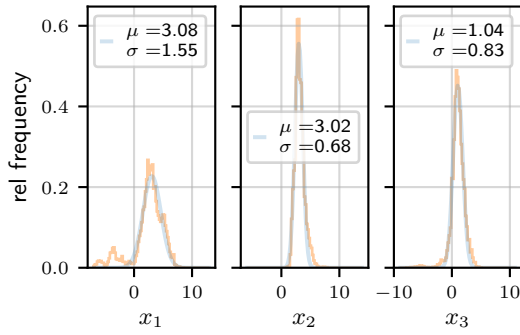


Fig. S19. (a) + (b) Parameters Histograms and fits $\mathcal{N}(\mu, \sigma)$ presenting the estimated simulation parameters λ_i for both networks in an ideal Kirchhoff network, dual Laves-Graph topology, multi-source-multi-sink system, rescaled axis is $x_i = \log_{10} \lambda_i$, the system was initialised symmetrically with $x_1 = 1$, $x_2 = 6$ and $x_3 = -$

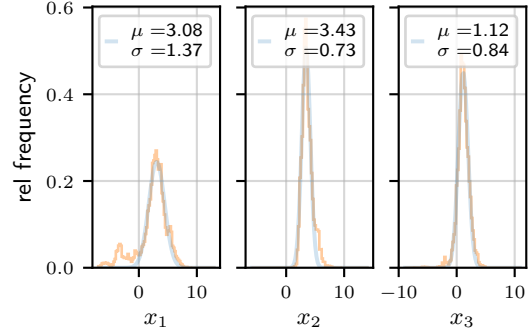
61 For experimental data sets such as sinusoids and bile canaliculi we crop a segment of the two networks in proximity of the
 62 central vein and 'clean' it up. First we identify the vertices in the sinusoidal network which are closest to the central vein (CV)
 63 according to the given segmentation. These vertices will be declared sinks while all other vertices in the sinusoidal section will
 64 be declared sources, which will be the fluctuating elements. We also now consider multiple sinks, which are set identical in
 65 their dynamics for computational simplicity, see supplement. We calculate their center of mass (CMS) and use it as the center
 66 of sphere of radius R. All other vertices and edges of either the sinusoidal or the canaliculi network which lie inside this sphere
 67 are the only components to be considered for future analysis. Other components outside the range of interest as well as edges
 68 penetrating the sphere's surface are discarded. We next identify all branching points in the sinusoidal network and all paths
 69 $\mathbf{p} = (e_i, \dots, e_j)$ consisting of edges e_i which start from these points. We proceed for the canaliculi the same way, and then check
 70 for each segment of a path whether there is another segment of another network's path inside a perimeter δ . If so, these paths
 71 count as affiliated and we define a distance between affiliated paths by calculating the minimal distance between two segments
 72 of these paths. For a reference length L we use the minimal distance found between the two networks (as we did before by
 73 using the lattice constants in the simulations). Then we coarse-grain the network of interest by merging all edges along a path.
 74 In practice this means that we use the conventional addition theorems for series of conductivities, $\frac{1}{\kappa_{eff}} = \sum_i \frac{1}{\kappa_i}$ and assuming
 75 an identical viscosity all across a network.



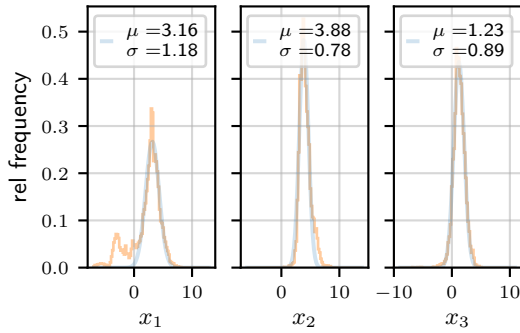
(a)



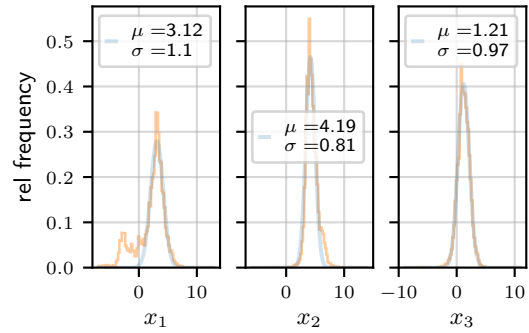
(b)



(c)



(d)



(e)

Fig. S20. Perimeter δ dependency of the estimated adaptation parameters in sinusoids: (a) Histogram displaying the number of affiliated neighbors(edges) found for a given radius around a vessel (threshold, all values the inset in μm). Total number of pairings found overall for given threshold in the inset. The 'carving radius' is $397\mu m$ as in the articles main part. (b) $\delta = 20\mu m$ (c) $\delta = 25\mu m$ (d) $\delta = 30\mu m$ (e) $\delta = 35\mu m$.

Finally this scheme could also be considered in the case of uncoupled networks $\lambda_1 = 0$, so that we may write this as,

$$\begin{aligned}
 1 &= \left(\frac{a_1}{a_0}\right) \left(\frac{\rho_1}{\rho_0}\right)^3 + \left(\frac{a_2}{a_0}\right) \left(\frac{\rho_2}{\rho_0}\right)^3 \\
 &= \sqrt{\frac{1 + \lambda_3 h_0}{1 + \lambda_3 h_1}} \left(\frac{\rho_1}{\rho_0}\right)^3 + \sqrt{\frac{1 + \lambda_3 h_0}{1 + \lambda_3 h_2}} \left(\frac{\rho_2}{\rho_0}\right)^3
 \end{aligned} \tag{60}$$

Subsequently one may solve the equation Eq. (60) by setting $(\frac{\rho_1}{\rho_0})^3 = \rho_{10}$, $(\frac{\rho_2}{\rho_0})^3 = \rho_{20}$ and solve for the root of the polynomial,

$$0 = b_0 + b_1\lambda_3 + b_2\lambda_3^2 + b_3\lambda_3^3 + b_4\lambda_3^4 \quad [61]$$

with coefficients

$$b_0 = \rho_{10}^4 + \rho_{20}^4 - 2\rho_{10}^2 - 2\rho_{20}^2 - 1 \quad [62]$$

$$b_1 = 2\rho_{10}^4 (h_2 + h_0) + 2\rho_{20}^4 (h_1 + h_0) - 2\rho_{10}^2 (2h_2 + h_0 + h_1) - 2\rho_{20}^2 (2h_1 + h_0 + h_2) - 2h_0 \quad [63]$$

$$b_2 = \rho_{10}^4 (h_2^2 + 4h_0h_2 + h_0^2) + \rho_{20}^4 (h_1^2 + 4h_0h_1 + h_0^2) - 2\rho_{10}^2 (h_2^2 + 2h_0h_2 + 2h_1h_2 + h_1h_0) - 2\rho_{20}^2 (h_1^2 + 2h_0h_1 + 2h_1h_2 + h_2h_0) - 4h_0 (h_1 + h_2) + h_2^2 + h_1^2 + 2h_1h_2 \quad [64]$$

$$b_3 = \rho_{10}^4 (h_0h_2^2 + h_0^2h_2) + \rho_{20}^4 (h_0h_1^2 + h_0^2h_1) - 2\rho_{10}^2 (h_0h_2^2 + h_1h_2^2 + h_0h_1h_2) - 2\rho_{20}^2 (h_0h_1^2 + h_1^2h_2 + h_0h_1h_2) - 2h_0^2 (h_1 + h_2) + 2h_1h_2 (h_1 + h_2 - h_0) \quad [65]$$

$$b_4 = \rho_{10}^4 h_0^2 h_2^2 + \rho_{20}^4 h_0^2 h_1^2 - 2\rho_{10}^2 h_2^2 h_1 h_0 - 2\rho_{20}^2 h_1^2 h_2 h_0 + h_1^2 h_2^2 - 2h_0^2 h_1 h_2 \quad [66]$$

76 References

- 77 1. GARRETT BIRKHOFF and J B DIAZ. NON-LINEAR NETWORK PROBLEMS. *Quarterly of Applied Mathematics*, 13
- 78 (4):431–443, January 1956.
- 79 2. R J DUFFIN. Distributed and Lumped Networks. *Journal of Mathematics and Mechanics*, 8(5):793–826, 1959.
- 80 3. R Penrose. A generalized inverse for matrices. In *Proceedings of the Cambridge Philosophical Society*, pages 406–413.
- 81 Cambridge University Press, July 1955.
- 82 4. A Ben-Israel and A Charnes. Generalized inverses and the Bott-Duffin network analysis. *Journal of Mathematical Analysis*
- 83 *and Applications*, 7(3):428–435, 1963.
- 84 5. R Penrose. On best approximate solutions of linear matrix equations. In *Proceedings of the Cambridge Philosophical*
- 85 *Society*, pages 17–19, January 1956.
- 86 6. F P KELLY. Network Routing. *Philosophical Transactions of the Royal Society of London Series a-Mathematical Physical*
- 87 *and Engineering Sciences*, 337(1647):343–367, 1991.
- 88 7. Leo J Grady and Jonathan R Polimeni. *Discrete Calculus*. Applied Analysis on Graphs for Computational Science.
- 89 Springer Science & Business Media, July 2010.
- 90 8. G H Golub and V Pereyra. The Differentiation of Pseudo-Inverses and Nonlinear Least Squares Problems Whose Variables
- 91 Separate. *SIAM Journal on Numerical Analysis*, 10(2):413–432, April 1973.
- 92 9. Francis Corson. Fluctuations and Redundancy in Optimal Transport Networks. *Physical Review Letters*, 104(4):048704–4,
- 93 January 2010.
- 94 10. Henrik Ronellenfitsch and Eleni Katifori. The Phenotypes of Fluctuating Flow: Development of Distribution Networks in
- 95 Biology and the Trade-off between Efficiency, Cost, and Resilience. *arXiv.org*, page arXiv:1707.03074, July 2017.
- 96 11. Dan Hu and David Cai. Adaptation and Optimization of Biological Transport Networks. *Physical Review Letters*, 111(13):
- 97 H1706–5, September 2013.

How to Pare a Pair: Topology Control and Pruning in Intertwined Complex Networks.

Felix Kramer^{a,b,c} and Carl Modes^{b,c}

^aInternational Max Planck Research School for Cell, Developmental and Systems Biology, Dresden, Germany; ^bMax Planck Institut for Molecular Cell Biology and Genetics (MPI-CBG), Dresden, Germany; ^cCenter for Systems Biology Dresden (CSBD), Dresden, Germany

Recent work on self-organized remodelling of vasculature in slime-mold, leaf venation systems and vessel systems in vertebrates has put forward a plethora of potential adaptation mechanisms. All these share the underlying hypothesis of a flow-driven machinery, meant to prune primary plexi in order to optimize the system's dissipation, flow uniformity, or more, with different versions of constraints. Nevertheless, the influence of environmental factors on the long-term adaptation dynamics as well as the networks structure and function have not been fully understood. Therefore, interwoven capillary systems such as found in the liver, kidney and pancreas, present a novel challenge and key opportunity regarding the field of coupled distribution networks. We here present an advanced version of the discrete Hu-Cai model, coupling two spatial networks in 3D. We show that spatial coupling of two flow-adapting networks can control the onset of topological complexity given the system is exposed to short-term flow fluctuations. Further, our approach results in an alternative form of Murray's law, which incorporates local vessel interactions and flow interactions. This scaling law allows for the estimation of the parameters in lumped parameter models and respective experimentally acquired network skeletons.

Multilayer network | Murray's law | Pruning | Liver

Many recent studies on biological transportation networks have been focused on the hypothesis that vasculature is remodelled according to the flow-induced stress sensed by the cells making up the tissue (1). This self-organized process optimizes the structures for the task at hand (distributing oxygen and nutrients, getting rid of waste, carrying local secretion). The actual tissue response is dependent on the time-scales probed, as short-term changes usually concern rapid vessel diameter changes in response to pressure fluctuations or medication, while long-term effects e.g. due to metabolic changes may manifest in permanent diameter changes (2), usually leaving the vessel structure with a trade-off between efficiency and redundancy (3).

Particular focus has been directed to the remodelling of the capillary plexus and other rudimentary transport systems in the early developmental stages of organisms, i.e. by studying complex signalling cascades involving growth factors like VEGF in vascular systems of mammals (4) or auxin in plants (5). Yet, the onset of refinement seems to be correlated with mechanical stresses (such as shear flow) as has been shown in a variety of model organisms like chicken embryo(1, 6), zebrafish(7), leaves(8) and slime mold (9).

Early theoretical approaches by Murray (10, 11) posited that diameter adaptation would minimize the overall shear and power dissipation of the system. Recent models using global optimization schemes on expanded vessel networks (where diameter adaptation may lead to link pruning) involving random damage, flow fluctuations or rescaled volume costs were

able to account for the trade-off of shunting and redundancies (12–14). Further advances were made in empirical studies of local vessel dynamics, e.g. blood vessel systems (15–17) as well as derived by constructing Lyapunov functions (18) describing the networks' effective maintenance cost (19). It has further been shown that the outcomes of locally adapting networks are robust against variations of the initial topological structure (20) and that plexus growth and correlated flow fluctuations can provide elaborate hierarchies (3, 21). Many of these effects may also be seen in continuous adaptation models in porous media (22, 23). It is interesting and important to note here that these adaptation mechanisms may leave certain fingerprints in the form of scaling laws, both allometric (24) and geometric (25).

Reviewing these works, it becomes apparent that only single networks were studied, involving volume or metabolic constraints. We here focus on the development and function of multicomponent flow networks, which are influencing each other based on their spatial architecture. Biologically speaking, these are systems consisting primarily of blood vessels and a secondary entangled, interacting system as found for example in liver lobule (26–29), the kidney's nephrons (30, 31), the pancreas (32–34) or the lymphatic system (35). More generally, any complex spatial network in 3D can be thought of as being entangled with its environment via its spatial complement which itself has the character of a network. In this work we study the adaptation of two coupled spatial networks according to an advanced version of the discrete Hu-Cai model (19). Each network is subject to flow driven and volume-constrained optimization on its own. Meanwhile we introduce the networks' interaction in the form of a mutual repulsion of vessel surfaces preventing them from touching directly by their otherwise flow driven radius expansion. Though the onset of redundancy is primarily driven by the existence of fluctuations, we find mutual repulsion to greatly reduce the networks relative loop density. Time-lapse experiments (7) counting the pruning events and topology analysis on pruned structures (3, 36, 37) allow for some insights. We further generalize an important scaling law, which has been discussed again recently in this context (38): Murray's Law. This generalization enables us to predict the model parameters with high fidelity for Kirchhoff networks solely from a given graph topology and its edge radii distribution. In the same manner we find a reasonable estimation for the parameters in experimentally acquired data sets of sinusoids in the mouse's liver acinus.

Felix Kramer and Carl Modes designed research and wrote the paper. Research was performed by Felix Kramer.

The authors declare no conflict of interest.

²To whom correspondence should be addressed. E-mail: kramer@mpi-cbg.de, modes@mpi-cbg.de

1. Results

A. Spatial coupling stabilizes spanning trees in pruned networks with flow fluctuations..

We model flow distribution networks as a composition of m rigid cylindrical tubes (referred to as edges) of given length l and radius r carrying a laminar flow, which are linked together by n branching points (vertices). Further we assume the flow to be non-pulsatile and hence a constant pressure drop Δp over the tube defined by its entry- and terminal-point hydrostatic pressures. The fluid considered has viscosity η and by including no-slip boundary conditions one can derive the volume flow rate f as the Hagen-Poiseuille law $f = \left(\frac{\pi r^4}{8\eta l}\right) \Delta p$ (39). We assign a flow f_e , a pressure-drop Δp_e and a conductivity $c_e = \frac{f_e}{\Delta p_e}$ to every edge. Likewise we assign a source or sink s_j as well as a nodal pressure p_j to every vertex. For further calculation of the flows and pressures in such lumped networks see (40).

In order to model biological transport networks such as found in the liver lobule, see Figure 1a, we define a multilayer network consisting of two intertwined, yet spatially separate objects each consisting of edges e and e' , with designated vessel radii $r_e, r_{e'}$. As underlying graph topology we choose from the graph skeletons of the triply-periodic minimal surfaces P ('dual' simple cubic), D ('dual' diamond cubic) or G ('dual' Laves) (41) to acquire two symmetric intertwined networks. Here, we start to model each network as a simple cubic lattice, see Fig. 1b and 1c, for further comment on the other structures see the supplement. We define a local affiliation of edges: Every quadruple $\mathbf{q} = (e_i, e_j, e_k, e_l)$ of edges forming a loop in its respective network is bound to enclose an edge e'_n of the other network. We refer to all edges from the quadruple \mathbf{q} as 'affiliated' with e'_n and vice versa. Each edge in any network is affiliated with up to four other edges in the other network (this will naturally change for different graph topologies). As all these edges are simply tubes in our model, we define the distance between affiliated tube surfaces to be,

$$\Delta r_{ee'} = L - (r_e + r_{e'}) \quad [1]$$

where L is the initial distance of the abstract network skeletons (equal to distance in case of simultaneously vanishing radii). In order to model a system of blood vessels which is entangled with a secondary secreting vessel network, we postulate that the respective tube surfaces must not fuse or touch directly, i.e. having $\Delta r_{ee'} = 0$. We do not incorporate periodic boundaries. For the networks' optimization we follow the conventional ansatz of minimization of flow dissipation and network volume, while including flow fluctuations as in (19). Subsequently we begin by constructing a Lyapunov function $\Gamma \geq 0$ for the combined system:

$$\Gamma = \sum_e \left[\frac{f_e^2}{c_e} + a v_e \right] + \sum_{e'} \left[\frac{f_{e'}^2}{c_{e'}} + a' v_{e'} \right] + E \quad [2]$$

introducing an 'energy density' E for the respective tube surfaces of the network edges

$$E = \frac{b}{2} \sum_{ee'} F_{ee'} \Delta r_{ee'}^{1-\varepsilon} \quad [3]$$

$$\text{with } F_{ee'} = \begin{cases} 1 & \text{if edges } e \text{ and } e' \text{ affiliated} \\ 0 & \text{else} \end{cases} \quad [4]$$

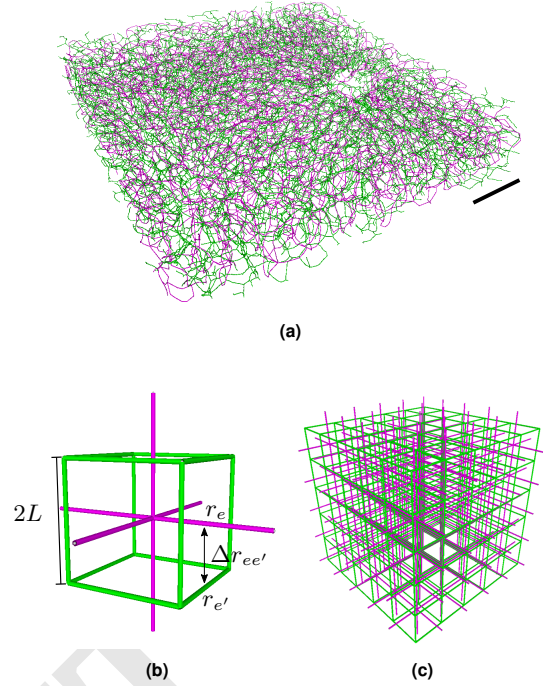


Fig. 1. (a) Biologically relevant intertwined structures: segment of bile canaliculi (green) and sinusoids (magenta) in the mouse's liver acinus (shown here as respective network skeletons, see also (29)). Scale bar is $200\mu\text{m}$. Modelling two interacting networks: (b) Unit cell and indication of spatial constraint for tube surfaces. (c) Periodic repetition of the unit cell as initial plexus.

As in (19) we consider a constant length scale l for all tubes, so we may rewrite the conductivity $k_e = l c_e = \frac{\pi}{8\eta} r_e^4$, which implies the changes of conductivity to be solely the result of radii adaptation. Additionally we set the volume penalty as $v_e = l r_e^2$. We define a pressure gradient as $\Delta \varphi_e = k_e^{-1} f_e$ where $k_e = \frac{\pi r_e^4}{8\eta}$ are elements of the diagonal \mathbf{K} . We do not consider cost variations via an exponent $k_e \rightarrow k_e^\gamma$ as suggested in other studies (12, 19). We may minimize Γ using a gradient descent method choosing the radii dynamics to be $\partial_t r_e = -\chi \nabla_{r_e} \Gamma$, and vice versa for $r_{e'}$ with auxiliary coefficients $\chi, \chi' > 0$. If a given radius falls below a set threshold we prune it, i.e. we remove the respective edge from the graph. Details of the derivation are given in the supplementary material.

Further we assume the adaptation of the vascular networks to depend on an averaged potential landscape instead of instantaneous configurations, which are bound to occur in real systems due to short-term metabolic changes or vessel blocking/damage. I.e. we assume a constant vessel radius between two adaptation events, while the flow rates change throughout the system due to changes in the sinks' magnitude. This incorporates the assumption of a time-scale separation between the radii adaptation (long-time changes, not to be confused with short term contraction/dilation) and changes of hydrostatic pressure. We define fluctuations in accordance to (14) and subsequently we update the ODE systems by substituting all occurrences $\Delta \varphi^2$ with $\langle \Delta \varphi^2 \rangle$. In this model all sink fluctuations are uncorrelated and follow the same probability distribution for every vertex j . Each sink has mean μ and standard deviation σ , see 'Materials and Methods'. In doing so we prevent shunting and the generation of spanning trees, which is caused by the typical 'single source - multiple sinks'

approach. Further, using this ansatz we prevent accidentally partitioning the Kirchhoff graph as opposed to realizing the sink-source configurations one by one (3).

In order to perform a numerical evaluation of the resulting ODE system we define the units as follows: the radii in units of the grids' distance $r_e = L\rho_e$, fluctuating nodal in and outflow $s_i = \mu\zeta_i$, time $t = h\frac{L^3}{\mu}$, the conductivity $k_e = \eta^{-1}L^4\kappa_e$ and hence pressure $\Delta\varphi_e = \frac{\mu\eta}{L^4}\Delta\Phi_e$ and the networks' edge surface distance $\Delta r_{ee'}^{-\varepsilon} = L^{-\varepsilon}\Delta\rho_{ee'}^{-\varepsilon}$. The ODEs may now be rescaled accordingly to the mean μ . The dimensionless form of the dynamical equations for each network is then of the form:

$$\frac{\partial_h \rho_e}{\lambda_0} = \sum_{jk} \alpha_{jk}^e [U_{jk} + \lambda_3 V_{jk}] \rho_e^3 - \lambda_2 \rho_e - \lambda_1 \sum_{e'} F_{ee'} \Delta \rho_{ee'}^{-\varepsilon} \quad [5]$$

with the effective temporal response parameters $\lambda_0 = \chi \left(\frac{\mu\eta}{L^3} \right)^2$, the effective network coupling $\lambda_1 = \frac{b(\varepsilon-1)}{\pi l \eta L^{\varepsilon+1}} \left(\frac{L^3}{\mu} \right)^2$ and the effective volume penalty $\lambda_2 = \frac{4a}{\pi \eta} \left(\frac{L^3}{\mu} \right)^2$. We incorporate flow fluctuations with the rescaled mean squared pressure $\langle \Delta\Phi_e^2 \rangle = \sum_{jk} \alpha_{jk}^e [U_{jk} + \lambda_3 V_{jk}]$ with $\alpha_{jk}^e = \kappa_e^{-1} [\mathbf{B} \cdot \boldsymbol{\kappa}^{1/2}]_{ej}^\dagger [\mathbf{B} \cdot \boldsymbol{\kappa}^{1/2}]_{ek}^\dagger$ and effective flow-fluctuation $\lambda_3 = \frac{\sigma^2}{\mu^2}$. The coefficient matrices \mathbf{U}, \mathbf{V} bear the information about the sinks-source cross correlations, see 'Materials and Methods' 3. The terms $\lambda'_0, \lambda'_1, \lambda'_2$ and λ'_3 , describing the second network with indices e' , are constructed analogously. To construct the networks in a symmetric manner we set the respective tube-lengths equally $l = l'$. The optimization according to Eq. (5) is performed until the edge radii reach a stationary state. During this optimization we mark edges whose radius falls below a critical threshold ρ_c . These edges are no longer updated and are considered to have a radius of virtually zero (though for computational reasons they are here set to $\rho_c = 10^{-21}$, these edges are referred to as pruned). The graphs consisting of m_c and m'_c non-pruned edges are then analyzed for its cyclic structure. We measure the number of the independent loops (nullity) in the final network as (42), assuming we never break our graph into multiple components. We calculate the relative nullity of a graph as $\varrho = \frac{m_c - n + 1}{l_0}$, where l_0 is the initial number of independent loops. The coefficients λ_2, λ'_2 play a negligible role in the systems final topology, as was noted in (19) and is explicitly shown in Figure 2 for the case of $\lambda_1 = \lambda'_1 = 0$. Note that the parameters λ_2, λ'_2 influence the final vessel diameter as well as the time scales for reaching the stationary state. With that being said, we focus our numeric studies on a systematic scan of the effective network coupling and flow-fluctuation parameters. For that purpose we set the fluctuation rates identical $\lambda_3 = \lambda'_3$ and scale the repulsion relative to each other as $\lambda_1 = \lambda'_1$. For our simulations we set the response $\lambda_0 = \lambda'_0 = 10^{-4}$, and volume penalty $\lambda_2 = \lambda'_2 = 10^6$ (which will provide us reasonable computation times for reaching a stationary state and prevent the problem becoming too stiff). The repulsion's exponent is set $\varepsilon = 2$. We solve the equations of motion Eq. (5) numerically with the Heun scheme using a manually adjusted increment of $h \leq 10^{-4}$ (decreasing time step for increasing λ_1). The initial edge radii are chosen randomly (with all affiliated edge pairs fulfilling $0 < \rho_e + \rho_{e'} < 1$).

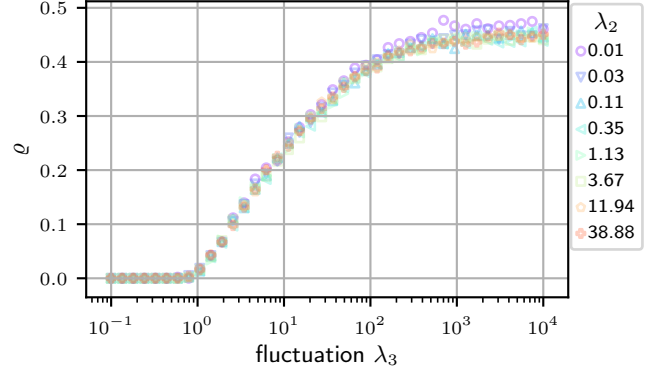


Fig. 2. An uncoupled adapting network displays a continuous, logarithmic λ_2 -independent nullity ϱ transition ($\lambda_1 = 0$, cubic lattice, $n = 216$ and $m = 540$).

All simulation results are presented here for one network only, as the results are highly symmetric. In Figure 3d we present the resulting nullity state diagram and its respective analysis. Refer to the supplement for the results of both networks in comparison as well as the respective results on their dynamics. Figure 3 shows that the nullity may be influenced not only by the rate of fluctuation λ_3 , but by the repulsion of the two networks as well. The nullity's transition is continuous, starting from a tree-like state ($\varrho = 0$) at small fluctuations and increasing monotonically in a logarithmic manner beyond a critical $\lambda_3 \geq \lambda^c$. Eventually, the ϱ -trajectory saturates for large fluctuation rates $\lambda_3 \geq \lambda^s$ towards a maximal nullity ϱ_{max} . The trajectories are altered regarding the onset of the transition as well as the saturation limit, see Figure 3e. To quantify these shifts we acquire the critical λ_c by identifying the logarithmic transition's root. The saturation λ_s is quantified by fitting the trajectories with a sigmoidal curve, providing us the possibility to extrapolate a saturation point which we define as $0.99\varrho_{max}$, see Figure 3f. It appears that the critical point λ_c becomes a monotonically increasing function in dependence of the coupling parameter λ_1 . In Figure 3g we show the rescaled trajectories of 3e near the onset of the nullity transition. Introducing the reduced fluctuation parameter $\epsilon = \frac{\lambda_3 - \lambda_c}{\lambda_c}$ we find the transition to follow a trivial logarithmic law $\varrho(\lambda_1, \lambda_3) \approx a(\lambda_1)(l\epsilon - 1)$, with the coupling dependent scale a shown in the inset of Figure 3g. Generating these state-diagrams for the respective D, G-skeletons we found no any qualitative differences arising from altered plexus topology.

B. Generalized form Murray's law allows estimation of adaptation parameters of real networks. Our model of spatial coupling also points to a new form of scaling at vessel branchings. We refer hereby to the concept by Murray's law, connecting the radii ρ_0 of the parent vessel splitting into at least two child branches with radii ρ_1, ρ_2 as:

$$\rho_0^\alpha = \rho_1^\alpha + \rho_2^\alpha \quad [6]$$

Originally a cubic scaling exponent $\alpha = 3$ was predicted (10) whereas relative costs models (12, 19) suggest

$$\alpha = 2(\gamma + 1) \quad [7]$$

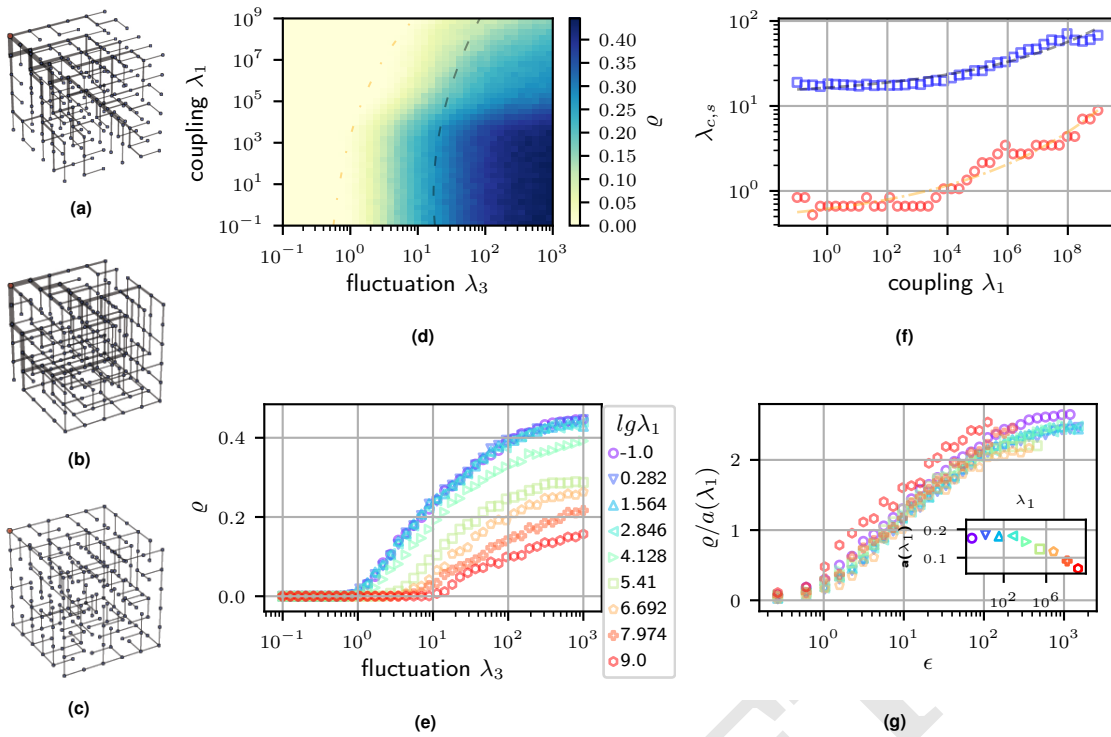


Fig. 3. Nullity ρ state diagram and network plots for a selected network: (a) $\lambda_1 = 1$, $\lambda_3 = 0.1$ (b) $\lambda_1 = 1$, $\lambda_3 = 10$ (c) $\lambda_1 = 10^9$, $\lambda_3 = 10$ (d) Coupling vs fluctuation, (λ_1, λ_3) -diagram, with nullity ρ color coded. Zones boundaries are representing the curves' fits from (f). (f) Critical λ_c (red circles) and saturation λ_s (blue squares) of coupling parameter λ'_1 . (e) For various coupling realizations ρ displays a logarithmic continuous transition and saturation. (g) Single curve collapse near nullity onset, with $\epsilon = \frac{\lambda_3 - \lambda_c}{\lambda_c}$ and scaled nullity $\rho/a(\lambda_1)$. We find the transition to follow $\rho(\lambda_1, \lambda_3) \approx a(\lambda_1)(\ln \epsilon - 1)$, the scale a is shown in the inset.

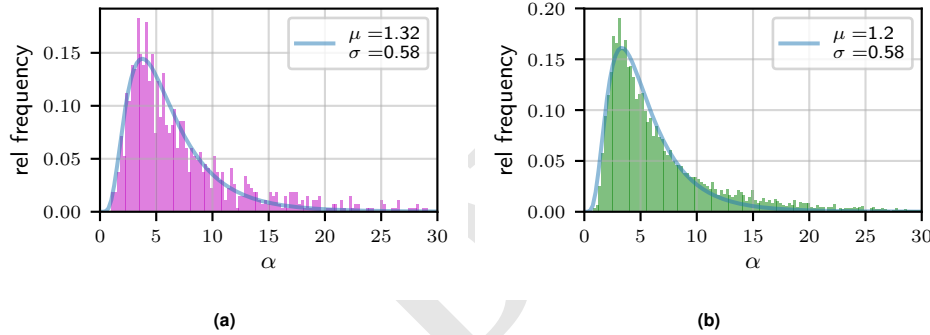


Fig. 4. Exponent distributions found for $\rho_0^\alpha = \rho_1^\alpha + \rho_2^\alpha$ and log-normal fit results in the insets: (a) Sinusoidal systems with maximum at $\alpha = e^\mu \approx 3.76$ and (b) bile canaliculi systems with maximum at $\alpha = e^\mu \approx 3.32$.

while discarding flow fluctuations. Testing these scaling laws for the network-skeletons of the sinusoids and bile canaliculi in the liver-lobule, by fitting the exponent α in Eq. (6) for every branching of degree three (Y-branching), one can see that there is significant deviation from the predicted exponent $\alpha = 3$, see Figure 4. The acquired values are $\alpha \approx 3.76$ for sinusoids and for bile canaliculi $\alpha \approx 3.32$. As capillary systems were already known to defy the cubic relationship (25), we suspect this to be correlated with the reticulated nature of these networks. Further, this deviation is not well described by the cost exponent γ . In accordance to Eq. (7) we would deduce γ to be smaller than one. Yet in this model's context the γ induced loop transition occurs at $\gamma \geq 1$ (12, 19) so the network would have to be a mere spanning tree to be valid. As the sinusoids and canaliculi are highly reticulated networks we propose that these loops are actually fluctuation induced (13, 14) and subsequently altered by the networks' mutual interaction. We can deduce from our pruning model a new set of coefficients a_j which are dependent on their corresponding edge's neighbourhood and the respective coupling strength, as

well as the global structure of sinks and sources (which were assumed to be uncorrelated and identically distributed). This procedure greatly alters the form of Eq. (6) and we derive a new scaling law derived from the steady-states of the ODEs in Eq. (5). We recover the cubic exponent of the original model with

$$\sum_e a_e \rho_e^3 = 1 \quad [8]$$

$$\text{with } a_e = \pm \sqrt{\frac{\lambda_2 + \lambda_1 \rho_e^{-1} \sum_{e'} F_{ee'} \Delta \rho_{ee'}^{-\epsilon}}{1 + \lambda_3 \frac{\sum_{jk} \alpha_{jk}^e V_{jk}}{\sum_{jk} \alpha_{jk}^e U_{jk}}}}$$

The scaling law Eq. (8) may also be generalized in case of more complicated flow landscapes, see supplement for derivation and discussion of Eq. (8). In this study we use the extracted graph skeletons of the sinusoids and bile canaliculi in the vicinity of a central vein in the mouse liver to test our model on a real intertwined vascular system. The vascular structure is thereby given to us by sets of vertices bearing the positional and radial

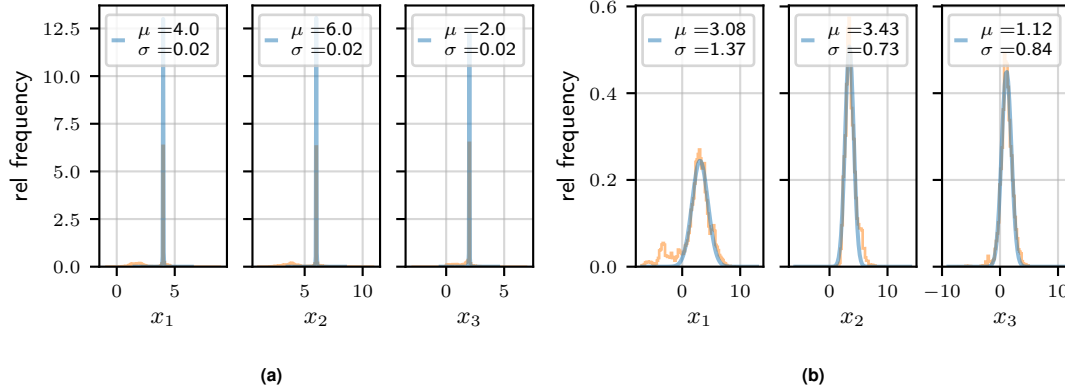


Fig. 5. Histograms and fits $\mathcal{N}(\mu, \sigma)$ presenting the estimated simulation parameters λ_i , rescaled axis is $x_i = \log_{10} \lambda_i$: (a) Parameters for an ideal Kirchhoff network, dual Laves-Graph topology, single source-multi sink system, the system was initialised symmetrically with $x_1 = 4$, $x_2 = 6$ and $x_3 = 2$ (b) Parameters for the sinusoidal system near the central vein, we found the distributions with mean values $x_1 = 3.08 \pm 1.37$, $x_2 = 3.43 \pm 0.73$, $x_3 = 1.12 \pm 0.84$.

information of the respective vascular sections, see Material and Methods.

B.1. Estimating parameters from ideal Kirchhoff networks. We tested the feasibility of ansatz Eq. (8) by simulating the pruning on a dual Laves graph topology (3-regular), with $n = 206$ ($n' = 210$) vertices and $m = 259$ ($m' = 261$) edges and setting the parameters symmetrically to $\lambda_1 = \lambda'_1 = 10^4$, $\lambda_2 = \lambda'_2 = 10^6$, $\lambda_3 = \lambda'_3 = 10^2$. The sources were positioned in random vertices of the system. Edges of the respective networks affiliated with each other similarly as before, though not by penetrating faces but by finding the first nearest neighbours of edges inside a perimeter δ . We numerically (43) find the roots of Eq. (8) for a set of positive definite $\lambda_1, \lambda_2, \lambda_3$ and $\lambda'_1, \lambda'_2, \lambda'_3$ respectively. As we do not intend to use information on the direction of the currents at the sink-nodes (and this information is not available in the real system) we will solve Eq. (8) for the seven relevant sign permutations at each branching, see supplement. For further evaluation only the fit of highest quality (function value) is used. We use a logarithmic rescaling $x_i = \log_{10} \lambda_i$ in order to find a symmetric representation of the histogram's data. Doing so we fit a normal distribution $\mathcal{N}(\mu, \sigma)$ to the distributions maximum and we find strong agreement with the actual parameters for both networks, see Figure 5a.

B.2. Estimating parameters for sinusoidal networks. We use the same approach to estimate the parameters $\lambda_1, \lambda_2, \lambda_3$ for the sinusoidal system in the liver lobule of mouse, based on the available information of topology and radii distribution. We first make some simplifying assumption about the position of sinks and sources as well as cropping the network-skeletons to remove degree two vertices, see Figure 6: First we identify the vertices in the sinusoidal network which are closest to the central vein (CV) and label them as sinks. We calculate their center of mass (CMS) and use it as the center of sphere of radius R (here chosen as $390 \mu m$). Any other components, vertices or edges outside this perimeter are discarded, see Figure 6a. We next identify all branching points in the sinusoidal network and all paths $\mathbf{p} = (e_i, \dots, e_j)$ consisting of edges e_i which start from these points. We proceed for the canaliculi the same way, see Figure 6b, and then check for each segment of a path whether there is another segment of another network's path inside a perimeter δ (here $25 \mu m$). If so, these paths count as affiliated, see supplement for further details. We merge all edges along a path towards a single

edge by using the conventional addition theorems for series of conductivities, see Figure 6b. Proceeding like this we end up with a reduced sinusoidal network, with $n = 318$ and $m = 452$. From this we calculate the repulsion and fluctuation terms in Eq. (8) and solve for the parameters again under consideration of all sign permutations for a_j . The solutions' histograms are presented in Figure 5b, where we find the parameters to be roughly distributed at $x_1 = 3.08 \pm 1.37$, $x_2 = 3.43 \pm 0.73$, $x_3 = 1.12 \pm 0.84$. In context of the nullity state diagrams we could place these in the transition zone, close to the border of the nullity-transition, see supplement. Yet, the large standard deviation and asymmetric character of the error (due to the logarithmic scaling) provide a certain level of uncertainty. Further, we found the choice of perimeters R, δ to interfere with the distributions presented in 5b. The imposed distribution of sources in the experimental system is also not strictly valid as one should only consider the vertices at the periphery as such.

2. Discussion

We have shown that spatial coupling presents another potential mechanism of controlling the topological complexity of optimal transport systems in 3D. Though the onset of redundancy is primarily driven by the existence of flow fluctuations, we have shown that mutual repulsion of vessel surfaces reduces the networks relative loop density and provides another method by which a system may tune its ultimate architecture. It's also possible to retrieve tree-like states at high fluctuation levels, which imposes a new stabilization mechanism for spanning trees in noisy networks. We considered the special case of 'single source to multiple sinks' in combination with simple cubic lattices as plexi as the simplest case possible. No qualitative differences could be found in the phase diagrams in comparison with the dual diamond, or dual Laves graphs. The Lyapunov ansatz provides a generally applicable tool in network optimization, and should properly be tested for other boundary conditions or graph geometries which resemble realistic structures.

Our model may also be seen as a toy-model for intertwined flow networks as found in the mammalian liver lobules and other related organ structures. Our approach further enabled us to derive a more general form Murray's law, directly involving flow interactions and environmental interactions. We find

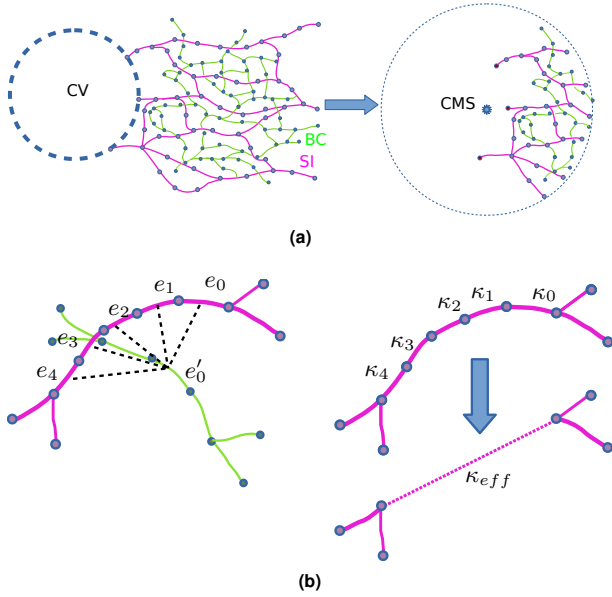


Fig. 6. Scheme of choosing the range of interest and coarse-graining the sinusoidal (SI) and bile canaliculi system (BC): (a) Left: Vertices lying closest to the central vein (CV) are identified as sinks. Right: We calculate the center of mass of all sinks (CMS) and take all vertices (and respective edges) inside a sphere of a given perimeter for our reduction into account. (b) Left: Deducing the respective distance of one path of a network to another path of the partner network by calculating the pair-wise distances of all path-segments and finding its minimum. If the minimum lies inside a give perimeter we count the edges as affiliated. Right: Coarse-graining paths consisting of nodes of degree two into one effective edge, which has the new edge weight according to addition theorem $\kappa_{eff} = \sum_i \frac{1}{\kappa_i}$

this technique to predict the interaction parameters with high fidelity for simulated Kirchhoff networks given their topology and respective edge radii distributions. In the same manner we find reasonable estimations for the parameters in experimentally acquired data sets of sinusoids in liver lobule of mice. Hence one could use this methodology as an effective classification of spatially adapting network structures. Apart from a refinement of the presented geometric coupling approach, an explicit involvement of hydrodynamic-chemical feedback between the distribution networks caused by the respective partner network should be taken into account: Biological systems such as the capillary networks in the liver lobule, present complex dual transport systems where the actual flow rates are not necessarily influenced by their respective partner network's flow rate (44) but rather by the concentration of bile salt components transported (27) as well as secretion rates of hepatocytes. Subsequently, future studies have to consider concentration/pump-rate dependent flow rate perturbations in the optimization model used so far, as well as a direct postulation of feedbacks in the adaptation dynamics to account for the actual network structures.

3. Materials and Methods

A. Sample Preparation, imaging and segmentation. Mouse livers from adult mice were fixed by trans-cardial perfusion, sectioned into 100 μm serial slices, optically cleared and immunostained, as described in (29). To visualize the different tissue components, the tissue sections were stained for nuclei (DAPI), cell borders (Phalloidin), bile canaliculi network

(CD13), and the extracellular matrix (ECM, fibronectin and laminin) facing the sinusoidal network(45). High-resolution images of the liver lobule (Central vein – portal vein axis) were acquired at by using confocal microscopy with a 63x/1.3 objective (0.3 μm voxel size). Finally, the resulting images were segmented and network skeletons calculated with the Motion Tracking software as described in (29) and (46).

B. Calculating currents and fluctuations in lumped networks.

Defining fluctuations in accordance to (14) we only consider s -configurations in which there exists one source-node (here $j = 0$) and all other nodes being sinks with the following characteristics:

$$\langle s_j \rangle = \mu_j \text{ with } j > 0 \quad [9]$$

$$\langle s_j s_k \rangle = \rho_{jk} \sigma_j \sigma_k + \mu_j \mu_k \text{ with } j, k > 0 \quad [10]$$

We assume the fluctuations are uncorrelated and follow the same probability distribution we have for the mean $\mu_j = \mu$, standard deviation $\sigma_j = \sigma$ and correlation coefficient $\rho_{jk} = \delta_{jk}$. Subsequently we may calculate the average squared pressure, writing:

$$\langle \Delta p_e^2 \rangle = \sum_{jk} A_{jk}^e [\mu^2 U_{jk} + \sigma^2 V_{jk}] \quad [11]$$

with coefficient matrices

$$V_{jk} = \delta_{jk} + (n + 1 + \delta_{jk}) \delta_{0j} \delta_{0k} - (1 + \delta_{jk}) (\delta_{0j} + \delta_{0k}) \quad [12]$$

$$U_{jk} = 1 + \delta_{0j} \delta_{0k} n^2 - n (\delta_{0j} + \delta_{0k}) \quad [13]$$

and with the auxiliary conductivity tensor $A_{jk}^e = c_e^{-1} [B \cdot C^{1/2}]_{ej}^\dagger [B \cdot C^{1/2}]_{ek}^\dagger$. It may be noted here that $A^e U$ describes the pressure p_e^2 in case of a constant source-sink landscape in the absence of any variance σ^2 . Hence $A^e V$ describes the pressure perturbation caused by fluctuations of strength σ^2 . For the full derivation of Eq. (11) and the respective coefficient matrices see the supplementary material.

ACKNOWLEDGMENTS. Our thanks go to Hernan Morales-Navarrete (image reconstruction) and Fabian Segovia-Miranda (experiments) for providing us with the sinusoidal and canaliculi skeleton datasets. We'd like to thank Marino Zerial, Julien Delpierre, Quentin Vagne, Dora Tang, Andre Nadler, Mark Werner and all members of the Modes Lab and Zechner Lab for their comments, helpful discussions and resourceful feedback during the process of creating this work and draft.

1. F LENOBLE, V FLEURY, A PRIES, P CORVOL, A EICHMANN, and R RENEMAN. Control of arterial branching morphogenesis in embryogenesis: go with the flow. *Cardiovascular Research*, 65(3):619–628, February 2005.
2. Dan Hu, David Cai, and Aaditya V Rangan. Blood Vessel Adaptation with Fluctuations in Capillary Flow Distribution. *PLoS ONE*, 7(9):e45444–, September 2012.
3. Henrik Ronellenfitch and Eleni Katifori. The Phenotypes of Fluctuating Flow: Development of Distribution Networks in Biology and the Trade-off between Efficiency, Cost, and Resilience. *arXiv.org*, page arXiv:1707.03074, July 2017.
4. W Risau. Mechanisms of angiogenesis. *Nature*, 386(6626):671–674, 1997.
5. Pavel Dimitrov and Steven W Zucker. A constant production hypothesis guides leaf venation patterning. *Proceedings of the National Academy of Sciences*, 103(24):9363–9368, June 2006.
6. Thi-Hanh Nguyen, Anne Eichmann, Ferdinand Le Noble, and Vincent Fleury. Dynamics of vascular branching morphogenesis: The effect of blood and tissue flow. *Physical Review E*, 73(6):6–14, June 2006.
7. Anna Lenard, Stephan Daetwyler, Charles Betz, Elin Ellertsdottir, Heinz-Georg Belting, Jan Huisken, and Markus Affolter. Endothelial Cell Self-fusion during Vascular Pruning. *PLOS Biology*, 13(4):e1002126–25, April 2015.

8. A Roth-Nebelsick. Evolution and Function of Leaf Venation Architecture: A Review. *Annals of Botany*, 87(5):553–566, May 2001.
9. Atsushi Tero, Ryo Kobayashi, and Toshiyuki Nakagaki. A mathematical model for adaptive transport network in path finding by true slime mold. *Journal of Theoretical Biology*, 244(4): 553–564, February 2007.
10. C D Murray. The Physiological Principle of Minimum Work: I. The Vascular System and the Cost of Blood Volume. *Proceedings of the National Academy of Sciences*, 12(3):207–214, March 1926.
11. Cecil D Murray. The Physiological Principle of Minimum Work. II. Oxygen Exchange in Capillaries. In *Proceedings of the National Academy of Sciences of the United States of America*, pages 299–304. Department of Biology, Bryn Mawr College, National Academy of Sciences, May 1926.
12. Steffen Bohn and Marcelo O Magnasco. Structure, Scaling, and Phase Transition in the Optimal Transport Network. *Physical Review Letters*, 98(8):088702–4, February 2007.
13. Eleni Katifori, Gergely J Szöllösi, and Marcelo O Magnasco. Damage and Fluctuations Induce Loops in Optimal Transport Networks. *Physical Review Letters*, 104(4):522–4, January 2010.
14. Francis Corson. Fluctuations and Redundancy in Optimal Transport Networks. *Physical Review Letters*, 104(4):048704–4, January 2010.
15. A R Pries, T W Secomb, and P Gaehtgens. Structural adaptation and stability of microvascular networks: theory and simulations. *American Journal of Physiology-Gastrointestinal and Liver Physiology*, 275(2):H349–H360, August 1998.
16. A R Pries, B Reglin, and T W Secomb. Structural adaptation of vascular networks - Role of the pressure response. *Hypertension*, 38(6):1476–1479, December 2001.
17. Timothy W Secomb, Jonathan P Alberding, Richard Hsu, Mark W Dewhirst, and Axel R Pries. Angiogenesis: An Adaptive Dynamic Biological Patterning Problem. *PLOS Computational Biology*, 9(3):e1002983–12, March 2013.
18. Volker Reitmann. *Reguläre und chaotische Dynamik*. Teubner, Stuttgart , Leipzig, 1996. ISBN 3815420903. URL http://slubdd.de/katalog?TN_libero_mab2442149.
19. Dan Hu and David Cai. Adaptation and Optimization of Biological Transport Networks. *Physical Review Letters*, 111(13):H1706–5, September 2013.
20. Johannes Gräwer, Carl D Modes, Marcelo O Magnasco, and Eleni Katifori. Structural self-assembly and avalanchelike dynamics in locally adaptive networks. *Physical Review E*, 92(1):290–7, July 2015.
21. Henrik Ronellenfitch and Eleni Katifori. Global Optimization, Local Adaptation, and the Role of Growth in Distribution Networks. *Physical Review Letters*, 117(13):H364–5, September 2016.
22. Jan Haskovec, Peter Markowich, and Benoît Perthame. Mathematical Analysis of a PDE System for Biological Network Formation. *Communications in Partial Differential Equations*, 40(5):918–956, 2015.
23. Jan Haskovec, Peter Markowich, Benoît Perthame, and Matthias Schlottbom. Notes on a PDE system for biological network formation. *Nonlinear Analysis*, 138:127–155, June 2016.
24. G B West. A General Model for the Origin of Allometric Scaling Laws in Biology. *Science*, 276(5309):122–126, 1997.
25. T F Sherman. On connecting large vessels to small. The meaning of Murray's law. *The Journal of general physiology*, 78(4):431–453, October 1981.
26. W Wayne Lauth. Regulatory processes interacting to maintain hepatic blood flow constancy: Vascular compliance, hepatic arterial buffer response, hepatorenal reflex, liver regeneration, escape from vasoconstriction. *Hepatology Research*, 37(11):891–903, November 2007.
27. James L Boyer. Bile formation and secretion. *Comprehensive Physiology*, 3(3):1035–1078, July 2013.
28. Kirstin Meyer, Oleksandr Ostrenko, Georgios Bourantas, Hernan Morales-Navarrete, Natale Porat-Shliom, Fabian Segovia-Miranda, Hidenori Nonaka, Ali Ghaemi, Jean-Marc Verbatatz, Lutz Brusch, Ivo Sbalzarini, Yannis Kalaidzidis, Roberto Weigert, and Marino Zerial. A Predictive 3D Multi-Scale Model of Biliary Fluid Dynamics in the Liver Lobule. *Cell Systems*, 4(3):277–290.e9, March 2017.
29. Hernan Morales-Navarrete, Fabian Segovia-Miranda, Piotr Klukowski, Kirstin Meyer, Hidenori Nonaka, Giovanni Marsico, Mikhail Chernykh, Alexander Kalaidzidis, Marino Zerial, and Yannis Kalaidzidis. A versatile pipeline for the multi-scale digital reconstruction and quantitative analysis of 3D tissue architecture. *Elife*, 4, 2015.
30. Mita M Shah, Rosemary V Sampogna, Hiroyuki Sakurai, Kevin T Bush, and Sanjay K Nigam. Branching morphogenesis and kidney disease. *Development*, 131(7):1449–1462, April 2004.
31. F C Serluca, I A Drummond, and M C Fishman. Endothelial signaling in kidney morphogenesis: A role for hemodynamic forces. *Current Biology*, 12(6):492–497, 2002.
32. Judith Magenheimer, Ohad Ilovich, Alon Lazarus, Agnes Klochendler, Oren Ziv, Roni Werman, Ayat Hija, Ondine Cleaver, Eyal Mishani, Eli Keshet, and Yuval Dor. Blood vessels restrain pancreas branching, differentiation and growth. *Development*, 138(21):4743–4752, November 2011.
33. Alethia Villasenor and Ondine Cleaver. Crosstalk between the developing pancreas and its blood vessels: an evolving dialog. *Seminars in Cell and Developmental Biology*, 23(6):685–692, August 2012.
34. D Berfin Azizoglu, Diana C Chong, Alethia Villasenor, Judith Magenheimer, David M Barry, Simon Lee, Leilani Marty-Santos, Stephen Fu, Yuval Dor, and Ondine Cleaver. Vascular development in the vertebrate pancreas. *Developmental Biology*, 420(1):67–78, December 2016.
35. Lara Planas-Paz and Eckhard Lammert. Mechanosensing in Developing Lymphatic Vessels. In *Developmental Aspects of the Lymphatic Vascular System*, pages 23–40. Springer Vienna, Vienna, November 2013.
36. Carl D Modes, Marcelo O Magnasco, and Eleni Katifori. Extracting Hidden Hierarchies in 3D Distribution Networks. *Physical Review X*, 6(3):031009–16, July 2016.
37. Lia Papadopoulos, Pablo Blinder, Henrik Ronellenfitch, Florian Klimm, Eleni Katifori, David Kleinfeld, and Danielle S Bassett. Comparing two classes of biological distribution systems using network analysis. *PLOS Computational Biology*, 14(9):e1006428–31, September 2018.
38. Dai Akita, Itsuki Kunita, Mark D Fricker, Shigeru Kuroda, Katsuhiko Sato, and Toshiyuki Nakagaki. Experimental models for Murray's law. *Journal of Physics D: Applied Physics*, 50(2): 024001–12, December 2016.
39. Lev Davidovich Landau and Evgenii Mikhailovich Lifshits. *Fluid Mechanics*, by L.D. Landau and E.M. Lifshitz, 1959.
40. Charles A. Desoer and Ernest S. Kuh. *Basic circuit theory*. McGraw-Hill, New York [u.a.], 1969. ISBN 0070165750. URL http://slubdd.de/katalog?TN_libero_mab214116274.
41. Wojciech T Gózdź and Robert Holyst. Triply periodic surfaces and multiply continuous structures from the Landau model of microemulsions. *Physical Review E (Statistical Physics, 54(5):5012–5027*, November 1996.
42. Hassler Whitney. Non-Separable and Planar Graphs. *Transactions of the American Mathematical Society*, 34(2):339–362, April 1932.
43. Eric Jones, Travis Oliphant, Pearu Peterson, et al. SciPy: Open source scientific tools for Python, 2001–. URL <http://www.scipy.org/>. [Online; accessed <today>].
44. R W BRAUER, G F LEONG, and R J HOLLOWAY. Mechanics of Bile Secretion - Effect of Perfusion Pressure and Temperature on Bile Flow and Bile Secretion Pressure. *American Journal of Physiology*, 177(1):103–112, 1954.
45. Hernan Morales-Navarrete, Hidenori Nonaka, André Scholich, Fabian Segovia-Miranda, Walter de Back, Kirstin Meyer, Roman L Bogorad, Victor Koteliangsky, Lutz Brusch, Yannis Kalaidzidis, Frank Jülicher, Benjamin M Friedrich, and Marino Zerial. Liquid-crystal organization of liver tissue. *Elife*, 8:1035, June 2019.
46. Hernan Morales-Navarrete, Hidenori Nonaka, Fabian Segovia-Miranda, Marino Zerial, and Yannis Kalaidzidis. Automatic recognition and characterization of different non-parenchymal cells in liver tissue. *2016 IEEE 13th International Symposium on Biomedical Imaging (ISBI)*, pages 536–540, April 2016.